Neurobiology of Disease

Basolateral Amygdala Hyperexcitability Is Associated with Precocious Developmental Emergence of Fear-Learning in Fragile X Syndrome

Matthew N. Svalina,[1,2,3,4] Christian A. Cea-Del Rio,[3,5] J. Keenan Kushner,[2,3] Abigail Levy,[3] Serapio M. Baca,[3] E. Mae Guthman,[2,3] Maya Opendak,[6,7] Regina M. Sullivan,[6,7] Diego Restrepo,[2,4*] and Molly M. Huntsman[2,3,8*]

[1]Medical Scientist Training Program, University of Colorado Anschutz Medical Campus, Aurora, Colorado 80045, [2]Neuroscience Graduate Program, University of Colorado Anschutz Medical Campus, Aurora, Colorado 80045, [3]Department of Pharmaceutical Sciences, University of Colorado Anschutz Medical Campus, Aurora, Colorado 80045, [4]Department of Cell and Developmental Biology, University of Colorado Anschutz Medical Campus, Aurora, Colorado 80045, [5]CIBAP, Escuela de Medicina, Facultad de Ciencias Medicas, Universidad de Santiago de Chile, Santiago, Chile 9170201, [6]Emotional Brain Institute, Nathan Kline Institute, Orangeburg, New York 10962, [7]Child Study Center, Child & Adolescent Psychiatry, New York University School of Medicine, New York, 10016, and [8]Department of Pediatrics, University of Colorado Anschutz Medical Campus, Aurora, Colorado 80045

Fragile X Syndrome is a neurodevelopmental disorder and the most common monogenic cause of intellectual disability, autism spectrum disorders, and anxiety disorders. Loss of fragile x mental retardation protein results in disruptions of synaptic development during a critical period of circuit formation in the BLA. However, it is unknown how these alterations impact microcircuit development and function. Using a combination of electrophysiologic and behavioral approaches in both male (*Fmr1*-/y) and female (*Fmr1*−/−) mice, we demonstrate that principal neurons in the *Fmr1*KO BLA exhibit hyperexcitability during a sensitive period in amygdala development. This hyperexcitability contributes to increased excitatory gain in fear-learning circuits. Further, synaptic plasticity is enhanced in the BLA of *Fmr1*KO mice. Behavioral correlation demonstrates that fear-learning emerges precociously in the *Fmr1*KO mouse. Early life 4,5,6,7-tetrahydroisoxazolo [5,4-c]pyridin-3ol intervention ameliorates fear-learning in *Fmr1KO* mice. These results suggest that critical period plasticity in the amygdala of the *Fmr1*KO mouse may be shifted to earlier developmental time points.

Key words: **basolateral amygdala; critical period; fear conditioning; fragile X syndrome; olfactory learning; synaptic plasticity**

Significance Statement

In these studies, we identify early developmental alterations in principal neurons in the Fragile X syndrome BLA. We show that, as early as P14, excitability and feedforward excitation, and synaptic plasticity are enhanced in Fmr1KO lateral amygdala. This correlates with precocious emergence of fear-learning in the *Fmr1*KO mouse. Early life 4,5,6,7-tetrahydroisoxazolo [5,4-c]pyridin-3ol intervention restores critical period plasticity in WT mice and ameliorates fear-learning in the *Fmr1*KO mouse.

Received Sep. 1, 2021; revised Aug. 2, 2022; accepted Aug. 5, 2022.

Author contributions: M.N.S., C.A.C.-D.R., S.M.B., M.O., R.M.S., D.R., and M.M.H. designed research; M.N.S., C.A.C.-D.R., J.K.K., and A.L. performed research; M.N.S., C.A.C.-D.R., A.L., and S.M.B. analyzed data; M.N.S. wrote the first draft of the paper; M.N.S., S.M.B., D.R., and M.M.H. edited the paper; M.N.S., D.R., and M.M.H. wrote the paper; S.M.B. and E.M.G. contributed unpublished reagents/analytic tools.

This work was supported by National Institutes of Health National Research Service Award Individual Predoctoral Fellowship F31 MH124277 to M.N.S.; National Institutes of Health Grants R01 DC000566 to D.R., R01 NS095311 to M.M.H., and R37 HD083217 to R.M.S.; National Science Foundation Graduate Research Fellowship DGE-1553798 to E.M.G.; and Universidad de Santiago de Chile, Vicerrectoría de Investigación, Desarrollo e Innovación DICYT 022001CDR to C.A.C.-D.R. We thank the University of Colorado Anschutz Medical Campus Behavioral Core for expertise and guidance on neonatal behavioral paradigms; and Optogenetics and Neural Engineering Core for expertise and guidance in the modification of the D.R. laboratory custom olfactometer.

*D.R. and M.M.H. contributed equally to this work as senior authors.

The authors declare no competing financial interests.

Correspondence should be addressed to Molly M. Huntsman at molly.huntsman@cuanschutz.edu.

https://doi.org/10.1523/JNEUROSCI.1776-21.2022

Copyright © 2022 the authors

Introduction

Fragile X syndrome (FXS) is an X-linked, monogenic neurodevelopmental disorder (NDD) characterized by intellectual disability, attention deficit hyperactivity disorder, and autism spectrum disorders (ASDs) (Hagerman et al., 2009). FXS is caused by a CGG repeat expansion mutation of the *FMR1* gene (Liu et al., 2018). Trinucleotide repeat expansion results in transcriptional silencing of the *FMR1* gene and subsequent loss of expression of the fragile x mental retardation protein (FMRP) (Fu et al., 1991). FMRP is an RNA binding protein with important regulatory functions during the transport and translation of target mRNAs (Chen et al., 2003; Darnell et al., 2011; Darnell and Klann, 2013). Further, FMRP is known to be differentially expressed during nervous system development and plays a key role in normal

cellular and synaptic development (Chen et al., 2003; Tessier and Broadie, 2008; Darnell et al., 2011; Bonaccorso et al., 2015; Doll and Broadie, 2015). Thus, loss of FMRP results in dysregulated protein synthesis with subsequent alterations in critical period (CP) induction and duration in FXS (Meredith et al., 2007; Bureau et al., 2008; Harlow et al., 2010; Till, 2010; Vislay et al., 2013).

Since the identification of the molecular pathophysiology underlying FXS (Fu et al., 1991; Verkerk et al., 1991), subsequent investigations have elucidated the functional role of FMRP in regulating synaptic plasticity (Zha, 2013) with several studies demonstrating impairments in homeostatic plasticity in FXS, a process essential for normal synaptogenesis during early development (Contractor et al., 2015). The precise balance between excitation and inhibition (E/I) is essential for maintaining homeostatic plasticity during normal development (Chaudhury et al., 2016). In NDDs like FXS, the timing and regulation of CPs are altered in early postnatal development by aberrant E/I balance (Rubenstein and Merzenich, 2003; Nelson and Valakh, 2015). These alterations in synaptic development during CPs manifest as the temporal onset of cognitive and behavioral deficits (Meredith, 2015). In FXS, marked CP dysfunction has been identified within multiple brain regions (Huber et al., 2002; Contractor et al., 2015), including the somatosensory cortex (He et al., 2014; Contractor et al., 2015) and the BLA (Olmos-Serrano et al., 2010; Vislay et al., 2013). Indeed, amygdala-based behaviors, including anxiety and fear disorders, are highly comorbid in individuals with FXS and ASDs (Tsiouris and Brown, 2004; Turk et al., 2005; Cordeiro et al., 2011). Further, alterations in the BLA have been postulated to be the leading cause of anxiety in FXS patients (Hagerman et al., 2009; Cordeiro et al., 2011).

Previous studies from our laboratory identified alterations of dendritic structure in adult excitatory principal neurons (PNs) (Olmos-Serrano et al., 2010) and synaptic function during early postnatal development in FXS (Vislay et al., 2013) in the BLA. In addition to alterations in BLA PNs, our laboratory has identified marked dysfunction in BLA interneurons during early postnatal development (Olmos-Serrano et al., 2010; Paluszkiewicz et al., 2011; Vislay et al., 2013; Cea-Del Rio and Huntsman, 2014; Martin et al., 2014). Thus, inhibitory neurotransmission defects in the BLA in *Fmr1*KO mice suggest that hyperexcitable circuitry may exacerbate amygdala-based behaviors in FXS (Olmos-Serrano et al., 2010, 2011). Interestingly, during the period of inhibitory synaptic development (P10-P21) (Huntsman and Huguenard, 2000), we observe a homeostatic enhancement of inhibitory function between P14 and P16 in the BLA of *Fmr1*KO mice (Vislay et al., 2013). These synaptic-level changes correspond with a well-defined sensitive time window in CP development underpinning the functional emergence of the amygdala in rodent models of fear-learning (Moriceau and Sullivan, 2005). Thus, it stands to reason that the window of effective CP plasticity may be altered (Meredith, 2015). However, despite the importance of the amygdala in the regulation of fear and fear responses, studies examining plasticity in emotional processing systems in early development in FXS are lacking.

To better understand the synaptic basis of behavioral changes in fear-learning during the sensitive period, we examined whether homeostatic changes in inhibitory function in early life coincide with changes in microcircuit development. In the present study, we combined whole-cell patch clamp electrophysiology and a developmentally appropriate classical Pavlovian odor-shock behavioral paradigm to explore the cellular, synaptic, circuit, and behavioral-level consequences of E/I balance alterations during a sensitive period in the amygdala CP. We found that during this time period excitatory PNs in the BLA demonstrate hyperexcitability. Further, we show that increases in evoked excitatory gain in the BLA coincides with enhanced synaptic plasticity in the *Fmr1*KO mouse. Behavioral correlation demonstrates that aberrant fear-learning emerges early in the *Fmr1*KO mouse. Early life 4,5,6,7-tetrahydroisoxazolo [5,4-c]pyridin-3ol (THIP) intervention restores early postnatal CP plasticity in the WT animal and ameliorates fear-learning in the *Fmr1*KO mouse. These results suggest that CP plasticity in the BLA of the *Fmr1*KO mouse may be shifted to earlier developmental time points and suggests synaptic scaling is inadequate to control excitatory gain during this time period. Thus, hyperexcitability may underpin the precocious emergence of amygdala function in the *Fmr1*KO mouse model of FXS.

Materials and Methods

Contact for reagent and resource sharing

Further information and requests for resources and reagents should be directed to and will be fulfilled by the Lead Contact, Molly M. Huntsman (molly.huntsman@CUanschutz.edu).

Experimental model and subject details

All experiments and procedures were conducted in accordance with protocols approved and reviewed by the Institutional Animal Care and Use Committee at the University of Colorado Anschutz Medical Campus, in accordance with guidelines from the National Institutes of Health. Slice electrophysiology experiments were conducted on mice aged PN days 14-16 (P14). Behavioral experiments were conducted on mice aged PN10 (days 8-10), P14 (days 14-16), and P21 (days 21-35). Experiments were conducted on both male (*Fmr1*-/y) and female (*Fmr1*−/−) mice. The following mouse lines were used in the experiments: C57Bl/6J (The Jackson Laboratory #000664) and FVB.NH (The Jackson Laboratory #001800) and B6.129P2-Fmr1^{tm1Cgr}/J (The Jackson Laboratory #003025) and FVB.129P2-Pde6b^{+}Tyr$^{c\text{-}ch}$Fmr1^{tm1Cgr}/J (The Jackson Laboratory #004624). All mice were obtained from The Jackson Laboratory and housed in polypropylene cages with wood shavings with a modified 10/14 h light/dark cycle. Food and water were available *ad libitum*.

Acute slice preparation for electrophysiology

Mice aged P14-P16, were first anesthetized with carbon dioxide (CO_2) and decapitated. Brains were quickly removed by dissection and glued cerebellar side-down on a vibratome (Leica Biosystems) stage and immersed in an ice-cold and oxygenated cutting solution (95% O_2/5% CO_2; in mM as follows: sucrose, 45; glucose, 25; NaCl, 85; KCl, 2.5; NaH_2PO_4, 1.25; $NaHCO_3$, 25; $CaCl_2$, 0.5; $MgCl_2$, 7; osmolality, 290-300 mOsm/kg). Acute coronal slices (300 μm) were prepared using a perpendicular cut in the rostral-caudal axis at the caudal end of the brain Leica vibratome. Slices containing BLA were incubated in oxygenated (95% O_2/5% CO_2) ACSF (in mM: glucose, 10; NaCl, 124; KCl, 2.5; NaH_2PO_4, 1.25; $NaHCO_3$, 25; $CaCl_2$, 2; $MgCl_2$, 2; osmolality 290-300 mOsm/kg) at 36°C for at least 30 min. All reagents were purchased from Sigma-Aldrich.

Electrophysiology

Slices were submerged in the slice chamber of a moving stage microscope (Scientifica; Olympus) equipped with 4× (0.10 NA) and 40× (0.80 NA) objectives, differential interference contrast optics, infrared illumination, LED illumination (CoolLED), a CoolSNAP EZ camera (Photometrics), and Micro-Manager 1.4 (Open Imaging), and continuously perfused with ACSF heated to 32°C-37°C at a rate of 2 ml/min. Whole-cell patch-clamp recordings were made using borosilicate glass pipettes (2.5-5.0 MΩ; King Precision Glass) filled with intracellular recording solution. Data were acquired with a Multiclamp 700B amplifier and were converted to a digital signal with the Digidata 1440 digitizer using pCLAMP 10.6 software (Molecular Devices). Recordings were obtained from visually identified excitatory PNs in the BLA. PNs were targeted based on their large, pyramidal-like soma. PN identity was

confirmed by examining neuron responses to brief (600 ms) depolarizing and hyperpolarizing current pulses. Typically, PNs fire broad action potentials (APs) separated by long afterhyperpolarizing potentials (AHPs), and show significant AP frequency adaptation when firing continuously (Sah et al., 2003). Recordings were terminated if the physiology of the neuron was inconsistent with BLA PNs (e.g., high membrane resistance, narrow AP halfwidth, large and fast spontaneous EPSCs).

For voltage-clamp experiments, a cesium methanesulfonate (CsMe)-based intracellular solution was used (in mM as follows: CsMe, 120; HEPES, 10; EGTA, 0.5; NaCl, 8; Na-phosphocreatine, 10; QX-314, 1; MgATP, 4; Na_2GTP, 0.4; pH to 7.3 with CsOH; osmolality adjusted to ~290 mOsm/kg). For all current-clamp and plasticity experiments, a potassium gluconate based intracellular solution was used (in mM as follows: potassium gluconate, 135; HEPES, 10; KCl, 20; EGTA, 0.1; MgATP, 2; Na_2GTP, 0.3; pH to 7.3 with KOH; osmolality adjusted to ~295 mOsm/kg). Access resistance was monitored throughout the experiments, and data were discarded if access resistance exceeded 25 MΩ or varied by >±20%. No junction potential compensation was performed. Data were sampled at 10 kHz and lowpass filtered at 4 kHz. Offline, current data were filtered using either a third-order Savistky-Golay filter with a ±0.5 ms window or a 2 kHz lowpass Butterworth filter after access resistance was assessed. Mean traces were created by first aligning all events by their point of maximal rise (postsynaptic currents) and then obtaining the mean of all events.

Electrophysiology experimental design

Electrophysiological parameters have been previously described (Guthman et al., 2020).

Ramped current injections. Immediately after achieving whole-cell configuration, LA neurons were recorded at rest in current-clamp mode (I_{hold} = 0 pA). Following a 3 s baseline period, the holding current was linearly ramped from 0 to 400 pA over 2 s. Twenty-five sweeps of data were collected for each neuron, and the data were used to determine the resting membrane potential, AP threshold, and rheobase current of LA PNs.

Square current injections. Following ramped current injections, we recorded the responses of LA neurons to a series of square hyperpolarizing and depolarizing current injections. Before initiation of the series of current injections, V_m of the BLA neurons was adjusted to ~−70 mV. Each cell was subjected to two series of 600 ms square current injections: −100 to 100 pA at 10 pA intervals and −200 to 400 pA at 25 pA intervals. The data collected in these experiments were used to determine active and passive membrane properties of the neurons.

Spontaneous EPSCs/IPSCs. Spontaneous EPSCs (V_{hold} = −70 mV) and IPSCs (V_{hold} = 0 mV) in BLA PNs were recorded for 80 s each.

Input–output curves. Thalamic afferents from the internal capsule were stimulated using a bipolar stimulating electrode (FHC). We recorded evoked EPSCs (V_{hold} = −70 mV) and IPSCs (V_{hold} = 0 mV) from LA PNs in response to internal capsule stimulation. Experiments were conducted over a range of stimulation intensities (0 to 100 μA with a 10 μA interval).

Synaptic plasticity. Minimum sample sizes for plasticity studies were determined by power calculation for a continuous endpoint, two-independent sample study assuming a 20% difference in means based on previously published literature with an α of 0.05 and a power of 80%. For LTP experiments, we recorded AMPA-mediated EPSCs elicited by electrical stimulation of the internal capsule (stimulation frequency = 0.066 Hz) in BLA PNs from WT and *Fmr1*KO mice at P14-P16 (voltage-clamp configuration, V_{hold} = –80 mV) in the presence or absence of the $GABA_A$ receptor antagonist, gabazine (SR-95531, 10 μM in DMSO, Tocris Biosciences). Following a 5 min baseline recording, high-frequency electrical stimulation (HFS; 2 trains of 100 pulses delivered at 100 Hz, 20 s apart) was delivered to the internal capsule. EPSCs were measured for 20-45 min after HFS in the same way as baseline recordings. Synaptic strength was quantified as the integrated charge of each evoked EPSC. Change in synaptic strength was determined by normalizing the integrated charge of each EPSC recorded both before and after HFS to the average integrated charge of all baseline recordings (average normalized integrated charge of baseline = 100%). Successful LTP induction was defined as a significant increase in normalized integrated charge during the last 5 min (minutes 16-20) after HFS compared with baseline (minutes −5 to −1). Successful PTP induction was defined as a significant increase in normalized integrated charge during the first 5 min post-tetanus (minutes 1-5) after HFS compared with baseline (minutes −5 to −1).

Definitions of electrophysiological parameters

V_{rest}. V_{rest} was defined as the mean V_m (I_{hold} = 0 pA) during a 500 ms baseline across all sweeps in the ramped injection experiments.

AP threshold. AP threshold was defined as the voltage at which dV/dt exceeded 20 V/s. AP threshold was calculated at the first AP of each sweep in the ramped injection experiments.

Rheobase current. Rheobase current was defined as the mean current injected at AP threshold for the first AP across all sweeps in the ramped injection experiments.

Membrane resistance. Membrane resistance was defined as the slope of the best fit line of the *I–V* plot using the −100 pA to 100 pA (10 pA steps) series of current injections. Mean voltage response to each current injection step was defined as the difference between baseline mean membrane voltage (100 ms before current injection) and the mean membrane voltage during the 100 ms period from 50 ms after the start of the injection to 150 ms after the start of the current injection. This 100 ms window was chosen to allow for measurement of the change in V_m after the membrane had charged and before any potential HCN channel activation. The *I–V* plot was constructed using all current steps below rheobase.

Maximum firing rate (FR). Maximum FR was defined as the inverse of the interspike interval (ISI) during the first 200 ms of the most depolarizing current injection step before attenuation of AP firing was observed. Maximum FR was calculated using the −200 to 400 pA (25 pA steps) series of current injections.

AP amplitude. Amplitude of the AP was defined as the voltage difference between the peak of the AP and its threshold potential (set at dV/dt = 20 V/s). AP amplitude was calculated at the rheobase sweep of the −200 to 400 pA (25 pA steps) series of current injections.

AP halfwidth. AP halfwidth was defined as the time between the half-amplitude point on the upslope of the AP waveform to the half-amplitude point on the downslope of the AP waveform. AP halfwidth was calculated at the rheobase sweep of the 200 to 400 pA (25 pA steps) series of current injections.

AHP magnitude. AHP magnitude was defined as the difference between the most hyperpolarized membrane voltage of the AHP (occurring within 100 ms after AP threshold) and AP threshold. AHP magnitude and latency data were calculated at the rheobase sweep of the −200 to 400 pA (25 pA steps) series of current injections. ΔAHP data were calculated at the rheobase + 50 pA sweep of the −200 to 400 pA (25 pA steps) series of current injections.

AHP latency. AHP latency was defined as the time from AP threshold and the peak of the AHP.

ΔAHP. ΔAHP was defined as the difference between the first and last AHP (ΔAHP = AHP_{last} – AHP_{first}).

AP phase plot. The AP phase plot was obtained by plotting the rate of change of the mean AP for each cell from the rheobase sweep of the −200 to 400 pA (25 pA steps) series of current injections as a function of the corresponding membrane voltage.

Latency to first AP. AP latency was defined as the time from the initiation of the current injection to the peak of the first AP. AP latency was calculated at the rheobase sweep of the −200 to 400 pA (25 pA steps) series of current injections.

FR adaptation ratio. FR adaptation was defined as the ratio of the first and the average of the last two ISIs, such that FR adaptation = ISI_{first}/$meanISI_{last\ two\ ISI}$. FR adaptation was calculated at the rheobase 50 pA sweep of the −200 to 400 pA (25 pA steps) series of current injections.

AP broadening. AP broadening was defined as the ratio of the AP halfwidths of the first two APs (Broadening = $halfwidth_{second}$/$halfwidth_{first}$). AP broadening was calculated at the rheobase 50 pA sweep of the −200 to 400 pA (25 pA steps) series of current injections.

AP amplitude adaptation. AP amplitude adaptation was defined as the ratio of the AP amplitude of the average of the last three APs and the

first AP, such that AP Amplitude adaptation = $\text{meanAmplitude}_{\text{last 3 APs}}$/ $\text{Amplitude}_{\text{first AP}}$. AP amplitude adaptation was calculated at the rheobase 50 pA sweep of the −200 to 400 pA (25 pA steps) series of current injections.

Membrane decay τ. Membrane decay τ was determined by using a single exponential fit, $f(t) = Ae^{-t/\tau}$, to fit the change in V_m induced by a −100 pA sweep in the −100 to 100 pA (25 pA steps) series of current injections.

Hyperpolarization-induced sag. Hyperpolarization-induced sag was calculated using the equation, $\frac{V_{min} - V_{ss}}{V_{min} - V_{bl}} \times 100\%$, where V_{min} was defined as the most hyperpolarized membrane voltage during the current injection, V_{ss} was defined as the mean steady-state membrane voltage (last 200 ms of the current injection), and V_{bl} was defined as the mean baseline membrane voltage (100 ms before current injection). Hyperpolarization-induced sag was measured from the −200 pA current injection.

Rebound spikes. Rebound spikes were defined as the number of APs in the 500 ms following the −200 pA current injection.

sEPSC/sIPSC detection and amplitude. sEPSC/sIPSCs were detected by a combined template and threshold method. Briefly, a template was made by subsampling 10% of local peaks exceeding at least 6× or 7× (sEPSC or sIPSC, respectively) the median absolute deviation of a rolling baseline current (50 ms before the peak). The template current was then truncated from its 20% rise point through the end of the decay time constant for the template current. Next, all local peaks exceeding 6× or 7× the median absolute deviation of a rolling baseline current (50 ms before the peak) were collected. The template was then scaled to each individual putative sEPSC or sIPSC peak, and each peak was assigned a normalized charge integral relative to the template. Finally, a normalized charge integral cutoff was chosen to exclude obvious noise/nonphysiological events below a certain normalized charge integral. sEPSC amplitude was defined as the difference between the peak amplitude of each detected current and its corresponding baseline current. sEPSC/sIPSC amplitude for each cell was defined as the median peak amplitude for that cell. sEPSC/sIPSC frequency was defined as the inverse of the interevent intervals of the events. The frequency measure for each neuron was defined as the median of the sEPSC/sIPSC frequencies for that cell.

sEPSC/sIPSC 20%-80% rise time. The 20%-80% rise time was defined as the time it took an sEPSC or sIPSC to reach 80% of its peak amplitude from 20% of its peak amplitude. The 20%-80% rise time was calculated from the mean sEPSC/sIPSC of a given LA PN.

sEPSC/sIPSC τ_{Decay}. sEPSC τ_{Decay} was determined using a single exponential fit, $f(t) = Ae^{-t/\tau}$. IPSC τ_{Decay} was defined as the weighted time-constant of IPSC decay. Briefly, a double exponential fit, $f(t) = A_1e^{-t/\tau 1} + A_2e^{-t/\tau 2}$, was used to obtain the parameters to determine the weighted time-constant where $\tau_{\text{Weighted}} = (\tau_1A_1 + \tau_2A_2)/(A_1 + A_2)$. τ_{Decay} was calculated using the mean sEPSC or sIPSC trace for a cell.

EPSC/IPSC detection and amplitude, input–output curves. To determine the evoked EPSC and IPSC amplitudes across varying stimulus intensities, we first determined the peak time relative to the 100 μA stimulation. Then, we defined EPSC or IPSC amplitude as the maximum positive or negative deflection, respectively, from the mean current response within a window of 6 SDs of the peak time jitter.

Stimulation for half-maximum EPSC/IPSC amplitude. To get the half-maximum stimulation intensity and the slope of the input–output curve, we used the least squares method to fit a line to the EPSC/IPSC output relative to stimulation input. We only used input values that elicited non-zero EPSC/IPSC amplitudes to determine the best fit line. We then used this best fit line to find the stimulation intensity that was associated with 50% of the maximum EPSC/IPSC amplitude for the PN.

Input–output curve slope. We defined input–output slope as the slope of the line created with a least squares fit of the input–output curve.

Behavior

Sample size and power calculations

Minimum sample sizes for behavioral studies were determined by power calculation for a continuous endpoint, two-independent sample study assuming a 40% difference in means based on previously published literature with an α of 0.05 and a power of 80%.

Pavlovian odor-shock conditioning

*Fmr1*KO and WT control animals, aged PN8-10 (P10), PN14-16 (P14), and PN21-35 (P21), were randomly assigned with counterbalancing to one of three experimental conditions: odor only, unpaired odor-shock, or paired odor-shock using custom-made MATLAB software for the random assignment of variables that also blinds the experimenter to experimental conditions. Pups were removed from the nest and placed in the conditioning chamber maintained at a thermoneutral temperature and given a 10 min acclimation period before conditioning commenced. Trials were separated by an intertrial interval of 4 min. Pups in the paired condition received 8 pairings of exposure to a neutral odor (conditioned stimulus [CS], 1% isoamyl acetate, Sigma-Aldrich, 2 L/min) for 30 s and coterminating with a mild, 0.5 mA electric shock (unconditioned stimulus [US]) delivered through an electrode placed on the tail. Odor delivery and current delivery were controlled using a custom-made olfactometer and MATLAB software (A. Li et al., 2015). In the case of the unpaired conditioning controls, odor presentation and tail-shock were separated by at least 60 s. In the case of the odor-only condition, pups were exposed to a 30 s CS-odor delivery only. The intertrial interval was 4 min. Trainings lasted for 45 min after which pups were returned to the nest. In the case of threshold testing, all intervals and experimental conditions were reduced by 50%. For THIP treatment studies, P14 WT and *Fmr1*KO animals received intraperitoneal injections of THIP at a dose of 10 mg/kg (Borsini et al., 1986) or vehicle control, ddH_20 30 min before conditioning. Animals were conditioned as described above for threshold. All data collection and processing were conducted in a randomized and blinded manner.

Y-Maze Alteration Test

To quantify a rodent's willingness to explore novel environments, pups were subjected to the Y-maze alteration test (Todrank et al., 2011; Murthy and Gould, 2018). This test requires animals to choose to spend their time between one of two arms of a Y-maze. In one arm of the Y-maze was placed a socially familiar odor (bedding shavings) and the other arm contained a Kimwipe with 20 μl of the conditioned odor (CS), 1% isoamyl acetate. For mouse pups younger than P21, pups were placed at the decision point of a developmentally appropriate Y-maze containing two arms and a start box (with between-trial counterbalancing). Pup choices toward or away from the CS odor, indicating preference or aversion respectively, were recorded and quantified. Latency to decision was also quantified. For mouse pups P21-P30, pups were placed in the start box of the Y-maze and allowed to navigate freely. For mouse pups <P10 and P14-P16, pups were placed at the decision point of the Y-maze with between trial counterbalancing. Pups were given 60 s to choose an arm. For pups aged P21-P30, a response was considered a choice when the pups body entered the alleyway of the arm. For pups aged <P10, a response was considered a choice when the pup either oriented its head toward one arm or the other or when the pups body entered the alleyway of the arm. The experimenter was blind to experimental condition, and all data were only decoded for analysis.

Quantification and statistical analysis

Statistical analyses

All data analysis was performed using custom-written MATLAB code or GraphPad Prism. Normality of the data was assessed using the Anderson–Darling test. For assessment of whether a single group differed from a normal distribution centered around zero, a one-sample *t* test was used. For a test between two groups, a paired or unpaired *t* test was used where appropriate. For tests between two groups of non-normal data, a Mann–Whitney *U* test (MWU) was used where appropriate. For tests between three or more groups of normal data with one independent variable, a one-way ANOVA was used with Tukey–Kramer *post hoc* test to examine differences between groups. A Kruskal–Wallis test was used to examine differences between three or more groups of non-normal data with one independent variable. A Kruskal–Wallis test was used to examine differences between three or more groups of non-normal data with one independent variable. A MWU was used as a *post hoc* test following a significant result in a Kruskal–Wallis test and was corrected for multiple comparisons using the FDR method (Curran-Everett, 2000). The critical significance value was set to $\alpha = 0.05$ or was set to an FDR-corrected

Table 1. Differences in active and passive membrane properties among LA PNs in WT and Fmr1KO mice[a]

	WT PNs ([a]n = 18; [b]n = 19)		Fmr1KO PNs ([a]n = 27; [b]n = 19)			
	Mean/median	SEM/IQR	Mean/median	SEM/IQR	Statistical comparisons	z value, rank-sum
Resting membrane voltage (mV)[a]	−59.0742	± 1.7835	−52.0954	± 1.7034	$p = 0.0089$, unpaired t test	ci: [−12.1 - −1.84], tstat: −2.74, df: 43, SD: 8.37
Rheobase current (pA)[a]	87.8309	± 8.92	46.4283	± 3.22	$p = 9.4892e-06$, unpaired t test	ci = [24.8-58.04], tstat: 5.02,df: 43, SD: 27.1
AP threshold (mV)[a]	−28.1404	6.0520	−27.0483	9.2112	$p = 0.6514$, MWU	zval: −0.452, rank-sum: 394
Membrane resistance (MΩ)[b]	257.41	89.27	329.62	109.41	$p = 0.0042$, MWU	zval: −2.86, rank-sum: 272
$\tau_{Membrane}$ (ms)[b]	39.23	6.9767	43.76	17.6758	$p = 0.0154$, MWU	zval: −2.42, rank-sum: 287
Maximum FR (Hz)[b]	33.00	± 2.18	32.8733	± 1.53	$p = 0.9610$, unpaired t test	ci = [−5.27 - 5.53], tstat: 0.0493, df: 36, SD: 8.20
Spike frequency (Hz)[b]						
	0.00	0.00	0.00	0.00	$p = 1.00$	z: 0, rs: 370.5
	0.00	0.00	0.00	0.00	$p = 1.00$	z: 0, rs: 370.5
	0.00	0.00	0.00	0.00	$p = 0.6175$	z: −0.50, rs: 362
	0.00	0.00	0.00	4.21	$p = 0.1552$	z: −1.42, rs: 331
	0.00	3.10	6.98	8.62	$p = 0.0374$	z: −2.08, rs: 305
	0.00	10.23	12.09	13.43	$p = 0.0481$	z: −1.98, rs: 306
	6.85	12.40	14.97	9.87	$p = 0.0101$	z: −2.57, rs: 282
	9.43	9.80	18.54	9.53	$p = 0.0245$	z: −2.25, rs: 293
	13.18	8.81	21.68	9.33	$p = 0.0102$	z: −2.57, rs: 282
	16.43	11.38	24.51	5.88	$p = 0.0072$	z: −2.69, rs: 278
	18.52	10.64	27.62	8.53	$p = 0.009$	z: −2.61, rs: 281
	21.34	11.82	28.12	5.54	$p = 0.0072$	z: −2.69, rs: 278
	23.85	9.52	30.73	6.73	$p = 0.0382$	z: −2.07, rs: 299
	27.64	10.96	31.82	6.08	$p = 0.018$	z: −2.36, rs: 289
	28.34	11.53	33.03	5.12	$p = 0.17$	z: −1.37, rs: 323
	31.65	9.85	34.53	6.20	$p = 0.129$	z: −1.52, rs: 318
	31.23	10.57	35.26	8.29	$p = 0.7371$, MWU	z: −0.34, rs: 359
AP halfwidth (ms)[b]	1.47	± 0.0562	1.76	± 0.0855	$p = 0.0068$, unpaired t test	ci: [−0.501 - −0.0864], df: 36 t-stat: −2.87, SD: 0.315
Latency to first AP (ms)[b]	114.80	82.60	152.00	126.53	$p = 0.0961$, MWU	zval: −1.66, rank-sum: 313
FR adaptation[b]	0.50	± 0.042	0.51	± 0.029	$p = 0.7999$, unpaired t test	ci = [−0.115 - 0.0893], tstat: −0.255, df: 34, SD: 0.151
AP broadening[b]	1.47	± 0.0582	1.70	±0.0812	$p = 0.0248$, unpaired t test	ci = [−0.437 −0.0314], tstat: −2.342, df: 36, SD: 0.308
AP amplitude (mV)[b]	62.84	± 2.12	57.45	± 2.69	$p = 0.1240$, unpaired t test	ci = [−1.55 - 12.3], tstat: 1.57, df: 36, SD: 10.5
Amplitude adaptation[b]	0.95	0.0775	0.95	0.0888	$p = 0.7481$, MWU	zval: 0.321, rank-sum: 382
AHP magnitude (mV)[b]	19.01	3.4012	18.46	2.9289	$p = 0.7261$, WU	zval: 0.35, rank-sum: 383
DAHP (mV)[b]	−5.4016	3.2028	−3.2227	4.3274	$p = 0.0505$, MWU	zval: −1.96, rank-sum: 303
AHP latency (ms)[b]	50.3895	± 4.70	63.9009	± 4.67	$p = 0.0488$, unpaired t test	ci = [−26.95 −0.0748], tstat: −2.04, df: 36, SD: 20.4
Hyperpolarization-induced Sag (%)[b]	8.4436	± 1.35	7.4749	± 1.10	$p = 0.5824$, unpaired t test	ci = [−2.57- 4.51], tstat: 0.555, df: 36, SD: 5.38
Rebound APs[b]	0.00	0.00/0.00	0.00	0.00/0.00	$p = 1.00$, MWU	zval: 0, rank-sum: 370.5

[a]Normal data are mean ± SEM with differences tested using an unpaired t test.
[b]Non-normal data are median and IQR with differences tested using an MWU.

value (α_{FDR}) for multiple comparisons. All statistical tests were two-tailed. Unless otherwise stated, experimental numbers are reported as $n = x, y$ where x is the number of neurons and y is the number of mice. Statistical parameters are reported in Results, and figure legends display p values and sample sizes.

Data display

Data visualizations were created in MATLAB, GraphPad Prism, and Adobe Illustrator. Normal data are the mean ± SEM. Non-normal data are the median with error bars extending along the interquartile range.

Data and software availability

Data and code are available on request.

Results

*Fmr1*KO BLA PNs exhibit hyperexcitability during a sensitive period in amygdala development

To examine whether there are differences in the intrinsic biophysical properties of PNs, we performed whole-cell patch-clamp recordings in acute coronal brain slices containing the BLA in infant WT and *Fmr1*KO mice on postnatal days 14-16. This postnatal timeframe corresponds to a known sensitive period in the functional emergence of the amygdala (Moriceau and Sullivan, 2005). Recordings were made in PNs in the BLA, the subnuclei of the amygdaloid complex known to undergo plastic changes in response to Pavlovian fear-conditioning. In these experiments, we measured 18 membrane properties (Table 1) by examining neuron responses to both a rheobase ramp and brief (600 ms) depolarizing and hyperpolarizing current steps (see Materials and Methods). We observed significant differences in both active and passive membrane properties of *Fmr1*KO PNs compared with WT animals (for complete statistics, see Table 1). Specifically, brief depolarizing current pulses elicited increased spike frequencies as a function of injected current across the test range of 100-325 pA (Fig. 1*A*,*B*; Table 1). However, no differences in maximum FRs were observed in *Fmr1*KO PNs compared with WT control animals (Fig. 1*A*,*B*; for complete statistical analyses, see Table 1; unpaired t test: $p = 0.961$, data pooled from n_{WT} = 19 neurons, 4 mice, 4 males, 0 females, 2 litters; n_{Fmr1KO} = 19 neurons, 4 mice, 4 males, 0 females, 2) as spiking in *Fmr1*KO BLA PNs exhibited marked saturation at higher stimulus intensities. *Fmr1*KO PNs exhibited higher resting membrane potentials (V_{rest}) such that at baseline PNs

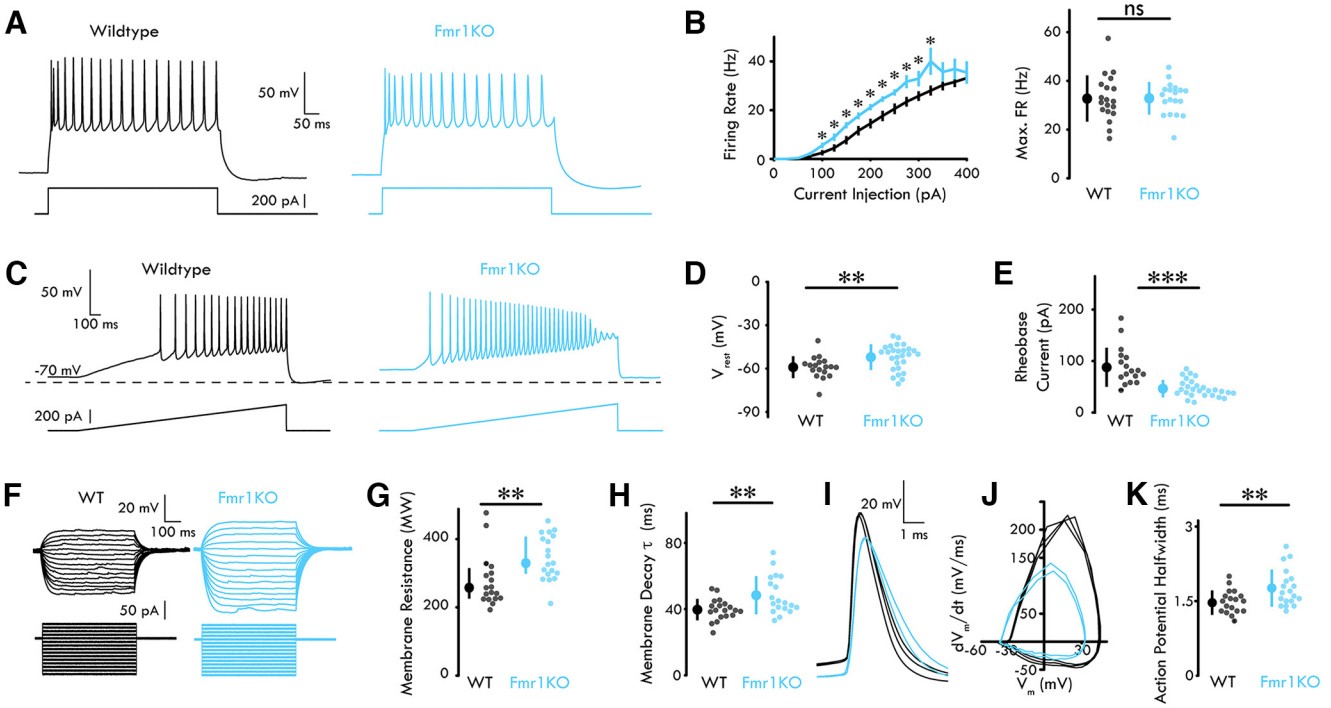

Figure 1. Membrane intrinsic properties are altered in PNs in the infant *Fmr1*KO BLA. ***A***, Representative traces of maximum FR response to depolarizing current injections in P14 WT and *Fmr1*KO LA PNs. ***B***, Left, Mean FR of BLA PNs. Error bars indicate SEM. *$p < 0.05$, spike frequencies found to be statistically significant at a given current injection. Spike frequency (Hz) values are detailed in Table 1. Right, Maximum FR of LA PNs is not significantly different in *Fmr1*KO compared with WT LA (unpaired *t* test: $p = 0.9610$; data pooled from $n_{WT} = 19$ neurons, 4 mice, 4 males, 0 females, 2 litters; $n_{Fmr1KO} = 19$ neurons, 4 mice, 4 males, 0 females, 2 litters). ***C***, Representative traces of voltage response to a ramped current injection in WT and *Fmr1*KO BLA PNs. ***D***, *Fmr1*KO BLA PNs have a more depolarized V_{rest} compared with WT BLA PNs (unpaired *t* test: $p = 0.089$; data pooled from $n_{WT} = 19$ neurons, 4 mice, 4 males, 0 females, 2 litters; $n_{Fmr1KO} = 19$ neurons, 4 mice, 4 males, 0 females, 2 litters). ***E***, *Fmr1*KO LA PNs exhibit a lower rheobase current from rest compared with WT BLA PNs (unpaired *t* test: $p = 9.49 \times 10^{-6}$; data pooled from $n_{WT} = 19$ neurons, 4 mice, 4 males, 0 females, 2 litters; $n_{Fmr1KO} = 19$ neurons, 4 mice, 4 males, 0 females, 2 litters). ***F***, Representative traces of voltage responses to intermediate current injection traces used to determine membrane resistance and decay τ (−100 to 100 pA; Δ10 pA). ***G***, Membrane resistance is increased in *Fmr1*KO BLA PNs compared with WT BLA PNs (MWU: $p = 0.0042$; data pooled from $n_{WT} = 19$ neurons, 4 mice, 4 males, 0 females, 2 litters; $n_{Fmr1KO} = 19$ neurons, 4 mice, 4 males, 0 females, 2 litters). ***H***, Membrane decay τ is increased in *Fmr1*KO LA PNs compared with WT BLA PNs (unpaired *t* test: $p = 0.0066$; data pooled from $n_{WT} = 19$ neurons, 4 mice, 4 males, 0 females, 2 litters; $n_{Fmr1KO} = 19$ neurons, 4 mice, 4 males, 0 females, 2 litters). ***I***, Representative AP traces from a WT and *Fmr1*KO BLA PN at rheobase current injection. ***J***, Representative phase plot traces from a WT and *Fmr1*KO BLA PN. ***K***, *Fmr1*KO LA PNs have broader AP halfwidths compared with WT BLA PNs (unpaired *t* test: $p = 0.0068$; data pooled from $n_{WT} = 19$ neurons, 4 mice, 4 males, 0 females, 2 litters; $n_{Fmr1KO} = 19$ neurons, 4 mice, 4 males, 0 females, 2 litters). ***B***, ***D***, ***E***, ***H***, ***K***, Summary statistics are mean ± SEM. ***G***, Summary statistics are median with IQR. *$p < 0.05$. **$p < 0.01$. ***$p < 0.001$. P14 = P14-P16. Complete statistical analyses reported in Table 1.

in in the BLA of *Fmr1*KO mice were found to be more depolarized. Further, *Fmr1*KO PNs exhibited a lower rheobase current (Fig. 1*C-E*: V_{rest}, unpaired *t* test: $p = 0.0089$; rheobase current: unpaired *t* test: $p = 9.49e\text{-}06$, data pooled from $n_{WT} = 19$ neurons, 4 mice, 4 males, 0 females, 2; $n_{Fmr1KO} = 19$ neurons, 4 mice, 4 males, 0 females, 2). Significant differences in passive membrane properties were also observed. *Fmr1* KO PNs exhibited increased membrane resistance (R_m) and membrane decay (τ) (Fig. 1*F-H*, R_m, MWU: $p = 0.0042$; decay τ, unpaired *t* test: $p = 0.0066$, data pooled from $n_{WT} = 19$ neurons, 4 mice, 4 males, 0 females, 2; $n_{Fmr1KO} = 19$ neurons, 4 mice, 4 males, 0 females, 2). No differences in membrane capacitance (C_m) were found between *Fmr1* KO and WT PNs. We also assessed properties of single APs (spike half-width, threshold, and amplitude). APs in *Fmr1*KO PNs demonstrated a larger half-width compared with WT animals (Fig. 1*I-K*, unpaired *t* test: $p = 0.0068$, data pooled from $n_{WT} = 19$ neurons, 4 mice, 4 males, 0 females, 2; $n_{Fmr1KO} = 19$ neurons, 4 mice, 4 males, 0 females, 2). Spike threshold and spike amplitude were comparable between groups (Table 1). Further, *Fmr1*KO PNs were found to have a longer AHP latency with no differences observed in the ΔAHP (ΔAHP, MWU: $p = 0.0505$; AHP latency, unpaired *t* test: $p = 0.0488$, data pooled from $n_{WT} = 19$ neurons, 4 mice, 4 males, 0 females, 2; $n_{Fmr1KO} = 19$ neurons, 4 mice, 4 males, 0 females, 2). Finally, we observed increases in AP broadening (Fig. 1*C*, AP broadening, MWU: $p = 0.0248$, data pooled from $n_{WT} = 19$ neurons, 4 mice, 4 males, 0 females, 2; $n_{Fmr1KO} = 19$ neurons, 4 mice, 4 males, 0 females, 2). No other membrane property comparisons reached statistical significance. Together, these data reveal significant increases in intrinsic hyperexcitability in *Fmr1*KO PNs compared with WT controls in the BLA of sensitive period animals.

Inhibitory synaptic strength is preferentially enhanced in the BLA of *Fmr1*KO mice

Previous studies from our group identified an enhancement of inhibitory neurotransmission such that the kinetics of IPSCs are transiently increased over the P14-P16 development time point (Vislay et al., 2013). One possible explanation for this enhancement could be that it is a homeostatic response to a concomitant increase in excitatory synaptic strength. However, our previous studies on synaptic transmission across development were done in the presence of NMDAR and AMPAR antagonists (D-APV and DNQX, respectively) to induce a complete excitatory blockade and isolate sIPSCs. Therefore, we could not assess the excitatory synaptic contribution to changes in inhibitory currents. Here we assessed sEPSCs and sIPSCs in visually identified PNs

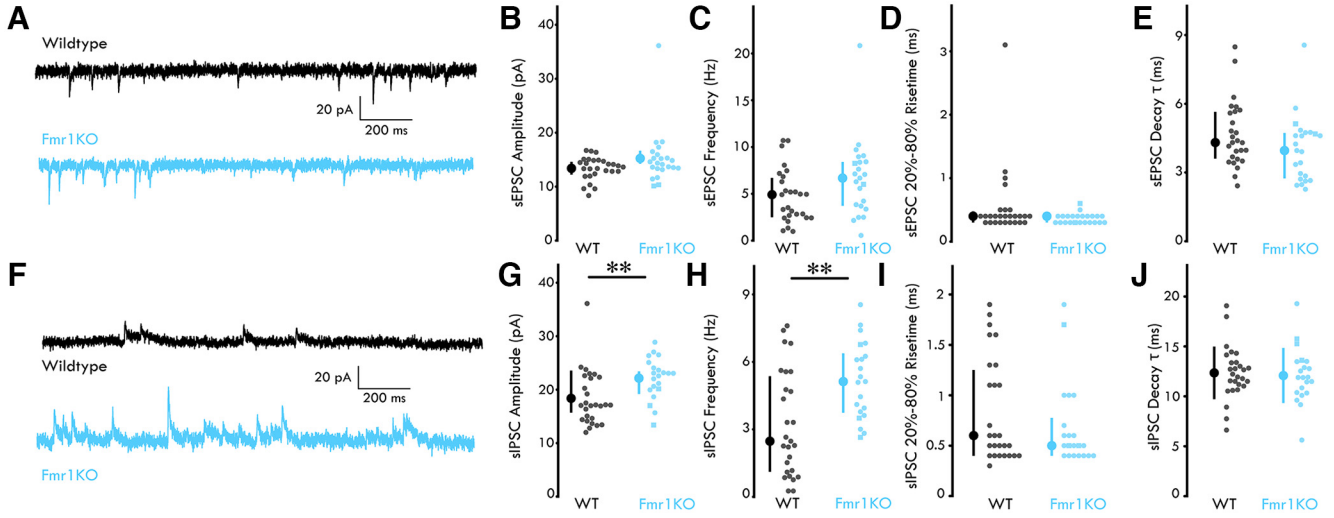

Figure 2. Enhanced spontaneous IPSCs in the *Fmr1*KO BLA. ***A***, Representative current traces from P14 LA PNs held at −70 mV. ***B***, No significant difference in sEPSC amplitude in LA PNs between WT and *Fmr1*KO mice (MWU: $p = 0.1289$; data pooled from $n_{WT} = 27$ neurons, 10 mice, 10 males, 0 females, 5 litters; $n_{Fmr1KO} = 23$ neurons, 10 mice, 8 male, 1 female, 6 litters). ***C***, No significant difference in sEPSC frequency in LA PNs between WT and *Fmr1*KO mice (MWU: $p = 0.0617$; data pooled from $n_{WT} = 27$ neurons, 10 mice, 10 males, 0 females, 5 litters, 5; $n_{Fmr1KO} = 23$ neurons, 10 mice, 8 males, 1 females, 6 litters). ***D***, No significant difference in sEPSC rise time in LA PNs between WT and *Fmr1*KO mice (MWU: $p = 0.1365$; data pooled from $n_{WT} = 27$ neurons, 10 mice, 10 males, 0 females, 5 litters; $n_{Fmr1KO} = 23$ neurons, 10 mice, 8 males, 2 females, 6 litters). ***E***, No significant difference in sEPSC decay τ in LA PNs between WT and *Fmr1*KO mice (MWU: $p = 0.1105$; data pooled from $n_{WT} = 27$ neurons, 10 mice, 10 males, 0 females, 5 litters; $n_{Fmr1KO} = 23$ neurons, 10 mice, 8 males, 2 females, 6 litters). ***F***, Representative current traces from P14 LA PNs held at 0 mV. ***G***, sIPSC amplitude is increased in LA PNs of *Fmr1*KO mice (MWU: $p = 0.0024$; data pooled from $n_{WT} = 27$ neurons, 11 mice, 11 males, 0 females, 6 litters; $n_{Fmr1KO} = 21$ neurons, 12 mice, 10 males, 2 females, 6 litters). ***H***, sIPSC frequency is increased in LA PNs of *Fmr1*KO mice (MWU: $p = 0.0032$; data pooled from $n_{WT} = 27$ neurons, 11 mice, 11 males, 0 females, 6 litters; $n_{Fmr1KO} = 21$ neurons, 12 mice, 10 males, 2 females, 6 litters). ***I***, No significant difference in sIPSC rise time in LA PNs between WT and *Fmr1*KO mice (MWU: $p = 0.4335$; data pooled from $n_{WT} = 27$ neurons, 11 mice, 11 males, 0 females, 6 litters; $n_{Fmr1KO} = 21$ neurons, 12 mice, 10 males, 2 females, 6 litters). ***J***, No significant difference in sIPSC decay τ is reduced in LA PNs between WT and *Fmr1*KO mice (unpaired *t* test: $p = 0.7326$; data pooled from $n_{WT} = 27$ neurons, 11 mice, 11 males, 0 females, 6 litters; $n_{Fmr1KO} = 21$ neurons, 12 mice, 10 males, 2 females, 6 litters). ***J***, Summary statistics are mean ± SEM. ***B-E***, ***G-I***, Summary statistics are median with IQR. $^*p < 0.05$. $^{**}p < 0.01$. P14 = P14-P16. Open circle represents male animal. Open square represents female animal. Complete statistical analyses are reported in Results.

in the BLA of *Fmr1*KO and WT animals using a cesium-methanesulfonate–based intracellular solution across the P14-P16 time point in the absence of the D-APV, DNQX, and the Na-channel blocker, TTX. We found no difference in sEPSC amplitude or frequency between *Fmr1*KO and WT PNs (Fig. 2*A-C*, sEPSC amplitude, MWU: $p = 0.129$, zval: 1.52, rank-sum: 767; sEPSC frequency, MWU: $p = 0.0617$, zval: −1.87, rank-sum: 592, data pooled from $n_{WT} = 27$ neurons, 10 mice, 10 males, 0 females, 5 litters; $n_{Fmr1KO} = 23$ neurons, 10 mice, 8 males, 1 female, 6). Spontaneous EPSC tau (τ) and 20%-80% rise time from *Fmr1*KO PNs did not differ from WT controls (Fig. 2*D*,*E*, sEPSC τ, $p = 0.111$, zval: 1.60, rank-sum: 771; sEPSC rise time, $p = 0.137$, zval: 1.49, rank-sum: 760). In accordance with our previous study (Vislay et al., 2013), we found a statistically significant increase in sIPSC amplitude and frequency for *Fmr1*KO PNs compared with WT PNs (Fig. 2*F–H*; sIPSC amplitude, MWU: $p = 0.0024$, zval: −3.03, rank-sum: 515); sIPSC frequency, MWU: $p = 0.0032$, zval: −2.95, rank-sum: 519; data pooled from $n_{WT} = 27$ neurons, 11 mice, 11 males, 0 female, 6 litters; $n_{Fmr1KO} = 21$ neurons, 12 mice, 10 males, 2 females, 6). No difference in sIPSC tau (τ) and 20%-80% rise time was found between *Fmr1*KO and WT controls (Fig. 2*I*,*J*; sIPSC τ, $p = 0.733$, ci = [−1.30 to 1.84], tstat: 0.344, df: 46, SD: 2.68; sIPSC rise time $p = 0.434$, zval: 0.783, rank-sum: 699). Together, inhibitory synaptic kinetics are preferentially enhanced both presynaptically and postsynaptically in *Fmr1*KO PNs without concomitant changes in excitatory synaptic strength.

Tonic inhibition represents a powerful inhibitory current that is mediated by $GABA_A$ receptor subunits (e.g., δ and $\alpha 3$ subunits) located outside of the synapse (Semyanov et al., 2004). To assess for differences in tonic inhibition between *Fmr1*KO and

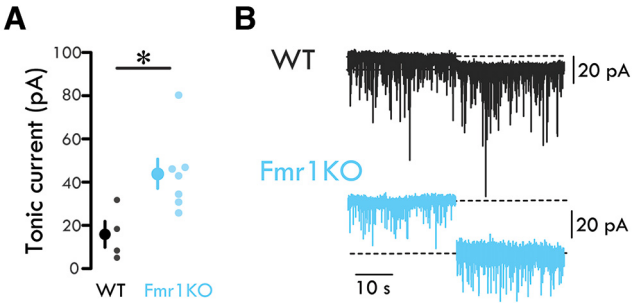

Figure 3. Tonic inhibition is enhanced in the *Fmr1*KO BLA. ***A***, Bar plots of pooled data of THIP activated tonic current (pA) in BLA PNs in WT and *Fmr1*KO mice at P14 (P14: unpaired *t* test, $p = 0.014$, data pooled from $n_{WT} = 4$ neurons, 2 mice, 2 males 0 females, 2 litters; $n_{Fmr1KO} = 7$ neurons, 3 mice, 3 male, 0 female, 3 litters). ***B***, Representative tonic current traces in WT and *Fmr1*KO BLA PNs at P14. ***A***, Summary statistics are mean ± SEM. $^*p < 0.05$. P14 = P14-P16. Complete statistical analyses are detailed in Results.

WT animals during the P14 sensitive period, we bath-applied the tonic-specific δ subunit agonist, THIP and assessed THIP-mediated tonic currents. At P14, tonic currents mediated through δ subunits in *Fmr1*KOs were significantly larger than WT levels (Fig. 3*A*,*B*; tonic current: unpaired *t* test, $p = 0.0221$, ci = [−50.97 to −5.06], tstat: −2.76, df: 9, SD: 16.2; data pooled from $n_{WT} = 4$ neurons, 2 mice, 2 males, 0 females, 2 litters; $n_{Fmr1KO} = 7$ neurons, 3 mile, 3 males, 0 females, 3). Similar to phasic inhibitory function (Vislay et al., 2013), tonic inhibition reverts back to reduced levels by P21 in *Fmr1*KOs (Martin et al., 2014). Together, these data show that two different forms of functional inhibition are transiently increased in *Fmr1*KOs at the P14-P16 time point relative to WT controls.

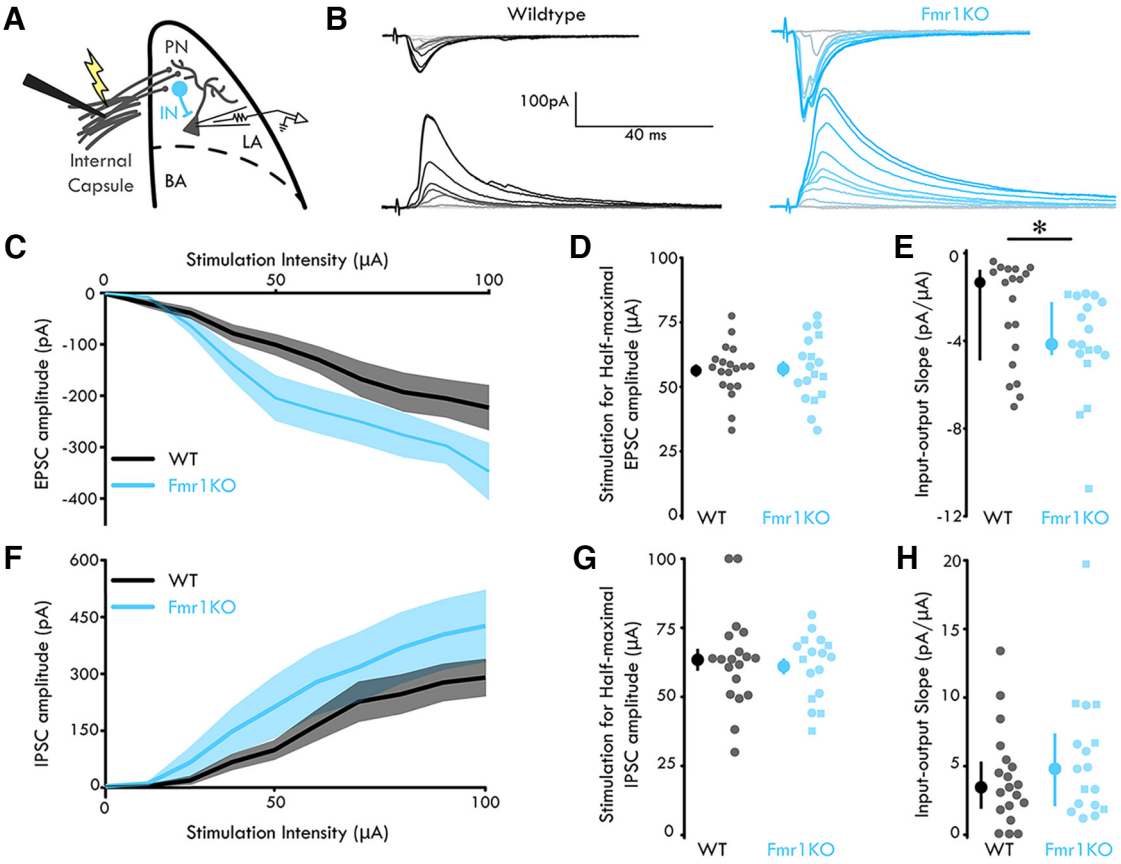

Figure 4. Enhanced excitatory gain in the *Fmr1*KO BLA. ***A***, Experimental schematic. ***B***, Representative mean traces of EPSCs (top) and IPSCs (bottom) in P14 LA PNs following internal capsule stimulation. Color scales with stimulation intensity (light to dark: 0-100 μA). ***C***, Mean evoked EPSC amplitude as a function of stimulation intensity. ***D***, Shading represents SEM. Stimulation for half-maximal EPSC amplitude is not significantly different for LA PNs from WT and *Fmr1*KO mice (unpaired *t* test: $p = 0.8618$; data pooled from $n_{WT} = 19$ neurons, 8 mice, 8 males, 0 females, 5 litters; $n_{Fmr1KO} = 18$ neurons, 8 mice, 6 males, 2 females, 5 litters). ***E***, Evoked EPSC input–output slope is significantly different in LA PNs in *Fmr1*KO mice (MWU *t* test: $p = 0.0403$; data pooled from $n_{WT} = 19$ neurons, 8 mice, 8 males, 0 females, 5 litters; $n_{Fmr1KO} = 18$ neurons, 8 mice, 6 males, 2 females, 5 litters). ***F***, Mean evoked IPSC amplitude as a function of stimulation intensity. ***G***, Shading represents SEM. Stimulation for half-maximal IPSC amplitude is not significantly different for LA PNs from WT and *Fmr1*KO mice (unpaired *t* test: $p = 0.3749$; data pooled from $n_{WT} = 19$ neurons, 8 mice, 8 males 0 females, 5 litters; $n_{Fmr1KO} = 17$ neurons, 8 mice, 6 males, 2 females, 5 litters). ***H***, Evoked IPSC input–output slope is not significantly different for LA PNs from WT and *Fmr1*KO mice (MWU: $p = 0.6363$; data pooled from $n_{WT} = 19$ neurons, 8 mice, 8 males, 0 females, 5 litters; $n_{Fmr1KO} = 17$ neurons, 8 mice, 6 males, 2 females, 5 litters). ***D***, ***G***, Summary statistics are mean ± SEM. ***E***, ***H***, Summary statistics are median with IQR. *$p < 0.05$. P14 = P14-P16. Open circle represents male animal. Open square represents female animal. Complete statistical analyses are detailed in Results.

Excitatory gain is enhanced in the BLA of *Fmr1*KO mice

In light of observed increases in the kinetics of spontaneous IPSCs, we hypothesized that increases in inhibitory synaptic strength may alter E/I microcircuit conductance in the infant BLA. To assess this, we quantified the amplitudes of evoked EPSCs and IPSCs in BLA PNs following stimulation of the thalamic sensory afferents of the internal capsule (Fig. 4*A*). We focused on the sensory afferents of the internal capsule because plasticity in this circuit underlies fear-learning (McKernan and Shinnick-Gallagher, 1997), and developmental changes in this circuit have been previously characterized (Thompson et al., 2008). Evoked EPSC and IPSCs were isolated in voltage clamp by holding at −70 and 0 mV, respectively (Fig. 4*B*). Synaptic input–output response curves were generated for both evoked EPSC and IPSCs over a stimulus intensity range of 10-100 μA (Fig. 4*C*,*F*). We found that feedforward excitatory drive onto PNs, as measured by the stimulation necessary to achieve half-maximal EPSC amplitude, was not different between groups (Fig. 4*C*,*D*; unpaired *t* test: $p = 0.8618$; zval: −0.0760, rank-sum: 358; data pooled from $n_{WT} = 19$ neurons, 8 mice, 8 males, 0 females, 5 litters; $n_{Fmr1KO} = 18$ neurons, 8 mice, 6 males, 2 females, 5 litters). However, the slope of the input–output function for *Fmr1*KO PNs was found to exhibit a significantly more negative slope (Fig. 3*C*,*E*; MWU *t* test: $p = 0.0403$, zval: 2.05, rank-sum: 429; data pooled from $n_{WT} = 19$ neurons, 8 mice, 8 males, 0 females, 5 litters; $n_{Fmr1KO} = 18$ neurons, 8 mice, 6 males, 2 females, 5 litters). However, a two-way ANOVA demonstrated statistically significant differences between groups for stimulation intensity and genotype, but not the interaction between intensity and genotype (Fig. 4*C*, two-way ANOVA $F_{(9,1,9)} = 20$, 21.21, 1.06, $p_{Intensity} =$ 4.43e-27, $p_{Genotype} =$ 5.78e-06, $p_{IntensityVGenotype} = 0.389$).

Similarly, the stimulation for half-maximal IPSC amplitude was not significantly different between groups (Fig. 4*F*,*G*; unpaired *t* test: $p = 0.375$, zval: −0.887, rank-sum: 323; data pooled from $n_{WT} = 19$ neurons, 8 mice, 8 males, 0 females, 5 litters; $n_{Fmr1KO} = 17$ neurons, 8 mice, 6 males, 2 females, 5 litters). Further, the slope of the IPSC input–output function was found to be broadly normal between the *Fmr1*KO and WT BLA PNs at P14 (Fig. 4*F*,*H*; MWU: $p = 0.636$, zval: 0.0159, rank-sum: 352.5; data pooled from $n_{WT} = 19$ neurons, 8 mice, 8 males, 0 females, 5 litters; $n_{Fmr1KO} = 17$ neurons, 8 mice, 8 males, 2 females, 5 litters). Two-way ANOVA demonstrated statistically significant differences between IPSC amplitudes for stimulation intensity

and genotype, but not the interaction between intensity and genotype (Fig. 4C, two-way ANOVA $F_{(9,1,9)} = 12.38, 11.56, 0.41$, $p_{Intensity}$ = 5.476e-17, $p_{Genotype}$ = 7.53e-4, $p_{IntensityVGenotype}$ = 0.931).

Together, these data indicate that feed-forward inhibition (FFI) in *Fmr1*KO BLA PNs is broadly normalized at this developmental time point. Further, similar amounts of activation of the thalamic afferents drive similar FFI and FFE onto BLA PNs in *Fmr1*KO and WT mice. However, once afferent activity is sufficient to elicit EPSCs and IPSCs in the postsynaptic PNs, the excitatory and inhibitory amplitudes increase to a larger degree as a function of afferent activity in the *Fmr1*KO mouse. This has the overall net effect of altering the input–output function such that significant increases in excitatory and inhibitory gain are present in the circuits necessary for fear-learning at this early developmental time point.

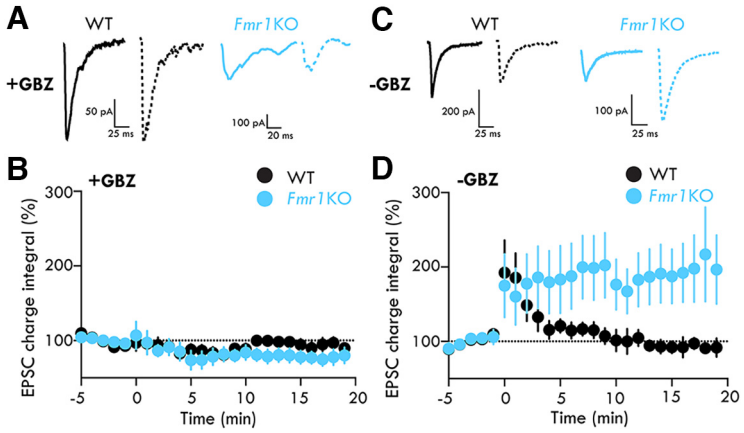

Figure 5. Aberrant LTP in *Fmr1*KO BLA. ***A***, Representative mean EPSCs from P14 LA PNs with 10 μM gabazine. Solid lines indicate mean EPSCs before LTP induction. Dashed lines indicate EPSCs at end of experiment. ***B***, Normalized EPSC charge integral across LTP experiments with 10 μM gabazine. One of six PNs underwent a small but significant LTP; 3 of 6 PNs underwent a small but significant LTD in WT BLA. Three of six PNs underwent significant LTD in the *Fmr1*KO BLA (paired *t* tests: p_{WT1} = 0.0063, p_{WT2} = 0.0098, p_{WT3} = 0.6225, p_{WT4} = 0.6487, p_{WT5} = 0.0476, p_{WT6} = 0.0373, $p_{Fmr1KO1}$ = 0.2948, $p_{Fmr1KO2}$ = 0.2390, $p_{Fmr1KO3}$ = 0.0001, $p_{Fmr1KO4}$ < 0.0001, $p_{Fmr1KO5}$ = 0.0003, $p_{Fmr1KO6}$ = 0.0649; n_{WT} = 6 neurons, 5 mice, 5 males 0 females, 4 litters; n_{Fmr1KO} = 6 neurons, 4 mice, 3 males, 1 female, 4 litters). ***C***, Representative mean EPSCs from P14 LA PNs without gabazine. Solid lines indicate mean EPSCs before LTP induction. Dashed lines indicate EPSCs at end of experiment. ***D***, Normalized EPSC charge integral across LTP experiments without gabazine. One of six PNs underwent significant LTP; 3 of 6 PNs underwent significant LTD in WT LA. Four of six PNs underwent LTP in *Fmr1*KO LA; 2 of 6 PNs underwent significant LTD in *Fmr1*KO LA (paired *t* tests: p_{WT1} = 0.00,346, p_{WT2} = 0.00,130, p_{WT3} = 0.0146, p_{WT4} = 0.1368, p_{WT5} = 0.8837, p_{WT6} = 0.4607, $p_{Fmr1KO1}$ < 0.0001, $p_{Fmr1KO2}$ = 0.0017, $p_{Fmr1KO3}$ = 0.0006, $p_{Fmr1KO4}$ = 0.0007, $p_{Fmr1KO5}$ = 0.0016, $p_{Fmr1KO6}$ = 0.00,280; n_{WT} = 6 neurons, 4 mice, 4 males 0 females, 4 litters; n_{Fmr1KO} = 6 neurons, 4 mice, 2 males, 2 females, 4 litters). Summary statistics are mean ± SEM. P14 = P14-P16. Complete statistical analyses are detailed in Results.

LTP in the presence of inhibition is robust in the BLA of *Fmr1*KO mice early in development

LTP is the mechanism mediating fear conditioning in the amygdala and local circuit GABAergic interneurons gate LTP in amygdala circuits associated with the processing of fearful memories. Enhancement of inhibition inactivates amygdala circuits and impairs fear conditioning, and it has been postulated that alterations in fear circuits may be a leading cause of anxiety in FXS patients. Because LTP is gated by FFI in the BLA and in light of our observations of preferential enhancements in inhibitory synaptic strength and normalization of FFI in the infant *Fmr1*KO BLA, we hypothesized that induction of LTP at synapses between thalamic afferents and BLA PNs would be reduced in *Fmr1*KO mice.

To test this hypothesis, we recorded AMPA-mediated EPSCs in PNs in the BLA of infant *Fmr1*KO and WT mice in the presence and absence of the $GABA_A$ receptor blocker gabazine (10 μM) (Fig. 5). Evoked EPSCs were elicited by electrical stimulation of the thalamic afferents of the internal capsule (voltage-clamp configuration, V_{hold} = –80 mV, stimulation frequency = 0.066 Hz, stimulation intensity = 50% of maximal evoked response per cell). Following a 5 min baseline recording, HFS (2 trains of 100 pulses delivered at 100 Hz, 20 s apart) was applied to the thalamic afferents of the internal capsule. When inhibition was blocked by gabazine, we did not find statistically significant LTP or LTD when evaluated for all experiments (Fig. 5*A*,*B* shows the mean difference ± SEM, paired *t* test for the EPSC charge integral, last 5 min $_{WTgrp}$, −6.17 ± 4.44%, p_{WTgrp} = 0.175 ci = [−15.2 to 2.91], tstat: 1.39, df: 29, SD: 24.30; n_{WT} = 6, 5). When evaluated on a per experiment basis, we observed a small magnitude LTP in 1 of 6 P14 WT PNs and LTD in 3 of 6 P14 WT PNs (Fig. 5*A*,*B*; paired *t* test EPSC charge integral$_{WT1}$ = 30.28 ± 7.32%, p_{WT1} = 0.0063, ci = [14.3-46.3], tstat: 5.25, df: 4, SD: 12.9; EPSC charge integral$_{WT2}$ = −17.6 ± 3.97%, p_{WT2} = 0.0098, ci = [−28.2 to −7.05], tstat: 4.63, df: 4, SD: 8.53; EPSC charge integral$_{WT3}$ = −3.01 ± 5.86%, p_{WT3} = 0.623, ci = [−18.7 to 12.7], tstat: 0.533, df: 4, SD: 12.6; EPSC charge integral$_{WT4}$ = −1.28 ± 2.73%, p_{WT4} = 0.649, ci = [−8.51 to 5.95], tstat: 0.492, df: 4, SD: 5.82; EPSC charge integral$_{WT5}$ = −8.19 ± 2.98%, p_{WT5} = 0.0476, ci = [−16.2 to −0.142], tstat: 2.84, df: 4, SD: 6.48; EPSC charge integral$_{WT6}$ = −37.2 ± 9.27%, p_{WT6} = 0.0373, ci = [−70.8 to −3.55], tstat: 3.07, df: 4, SD: 27.1). In P14 *Fmr1*KO PNs, we observed a robust LTD when statistical significance was evaluated for all experiments (Fig. 5*A*,*B*; paired *t* tests: EPSC charge integral, last 5 minutes$_{Fmr1KOgrp}$ −22.8 ± 4.10%, $p_{Fmr1KOgrp}$ < 0.0001, ci = [−31.2 to −14.4], tstat: 5.56, df: 29, SD: 22.5; n_{Fmr1KO} = 6, 4). When changes were evaluated on a per experiment basis, 3 of 6 P14 *Fmr1*KO PNs tested showed significant LTD (Fig. 5*A*,*B*; paired *t* test: EPSC charge integral$_{Fmr1KO1}$ = −0.173 ± 0.1139%, $p_{Fmr1KO1}$ = 0.2948, ci = [−0.572 to 0.226], tstat: 1.21, df: 4, SD: 0.321; EPSC charge integral$_{Fmr1KO2}$ = −10.99 ± 6.63%, $p_{Fmr1KO2}$ = 0.239, ci = [−33.1 to −11.1], tstat: 1.32, df: 4, SD: 17.8; EPSC charge integral$_{Fmr1KO3}$ = −63.7 ± 5.204%, $p_{Fmr1KO3}$ < 0.0001, ci = [−75.5 to −51.80], tstat: 14.9, df: 4, SD: 9.55; EPSC charge integral$_{Fmr1KO4}$ = 28.99 ± 2.422%, $p_{Fmr1KO4}$ < 0.0001, ci = [−33.99 to −23.98], tstat: 16.1, df: 4, SD: 4.03; EPSC charge integral$_{Fmr1KO5}$ = −21.97 ± 1.76%, $p_{Fmr1KO5}$ = 0.0003, ci = [−27.01 to −16.9], tstat: 12.1, df: 4, SD: 4.06). Between group analysis demonstrated a significant difference in LTD between P14 WT and *Fmr1*KO PNs (EPSC charge integral$_{Fmr1vsWT}$ = 15.7 ± 5.27%, $p_{Fmr1vsWT}$ = 0.0058, ci = [4.91-26.2], tstat: 2.98, df: 29, SD: 28.8, unpaired *t* test).

In contrast when local inhibition was not blocked, we found that in *Fmr1*KO mice LTP was statistically significant when evaluated on the basis of all experiments (paired *t* test: EPSC charge integral, last 5 minutes$_{Fmr1KOgrp}$ = 97.78 ± 19.40%, $p_{Fmr1KOgrp}$ < 0.0001, ci = [87.2-108.3], tstat: 25.7, df: 4, SD: 8.49, n_{Fmr1KO} = 6, 5). When evaluated on a per experiment basis, 4 of 6 *Fmr1*KO PNs underwent significant and robust LTP following HFS of thalamic afferents (Fig. 5*C*,*D*) with 2 of 6 *Fmr1*KO PNs undergoing significant LTD (paired *t* tests: EPSC charge integral$_{Fmr1KO1}$ = 187.5 ±

6.876%, $p_{Fmr1KO1} < 0.0001$, ci = [177.4-197.6], tstat: 51.7, df: 4, SD: 8.11; EPSC charge integral$_{Fmr1KO2}$ = 96.26 ± 12.41%, $p_{Fmr1KO2}$ = 0.0017, ci = [60.7-131.9], tstat: 7.51, df: 4, SD: 28.7; EPSC charge integral$_{Fmr1KO3}$ = 259.5 ± 37.2%, $p_{Fmr1KO3}$ = 0.0006, ci = [186.1-332.9], tstat: 9.82, df: 4, SD: 59.1; EPSC charge integral; $_{Fmr1KO4}$ = 80.7 ± 7.93%, $p_{Fmr1KO4}$ = 0.0007, ci = [57.2-104.2], tstat: 9.54, df: 4, SD: 18.9; $_{Fmr1KO5}$ = −20.5 ± 2.73%, $p_{Fmr1KO5}$ = 0.0016, ci = [−27.96 to −12.99], tstat: 7.60, df: 4, SD: 6.03; $_{Fmr1KO6}$ = −16.8 ± 3.66%, $p_{Fmr1KO6}$ = 0.0280, ci = [−30.6 to −2.96], tstat: 3.37, df: 4, SD: 11.11). In slices from WT mice in the absence of gabazine, we found no statistically significant LTP or LTD when evaluated for all experiments (Fig. 5*C*,*D*, paired *t* tests: EPSC charge integral, last 5 min $_{WTgrp}$ = −9.997 ± 4.94%, p_{WTgrp} = 0.0542, ci = [−20.2 to 0.195], tstat: 2.02, df: 24, SD: 24.7; n_{WT} = 6, 5). One of six WT BLA PNs underwent a small LTP, and 3 of 6 WT BLA PNs underwent small, but significant LTD (Fig. 5*C*,*D*; paired *t* tests: EPSC charge integral$_{WT1}$ = −32.96 ± 12.3%, p_{WT1} = 0.0346, ci = [−62.04 to −3.88], tstat: 3.15, df: 4, SD: 23.4; EPSC charge integral$_{WT2}$ = 22.9 ± 4.97%, p_{WT2} = 0.0130, ci = [8.02-37.8], tstat: 4.27, df: 4, SD: 12.01; EPSC charge integral$_{WT3}$ = −24.04 ± 6.13%, p_{WT3} = 0.0146, ci = [−40.2 to −7.85], tstat: 4.12, df: 4, SD: 13.04; EPSC charge integral$_{WT4}$ = −15.9 ± 7.51%, p_{WT4} = 0.137, ci = [−39.70 to 7.87], tstat: 1.86, df: 4, SD: 19.2; EPSC charge integral$_{WT5}$ = −0.000368 ± 0.002203%, p_{WT5} = 0.884, ci = [−0.0069 to 0.0062], tstat: 0.156, df: 4, SD: 0.0053; EPSC charge integral$_{WT6}$ = 6.82 ± 8.21%, p_{WT6} = 0.4607, ci = [−16.40 to 30.04], tstat: 0.815, df: 4, SD: 18.7). Between-group analysis demonstrated a significant difference in LTP between P14 WT and *Fmr1*KO PNs in the absence of $GABA_A$ receptor blockade (EPSC charge integral$_{Fmr1vsWT}$ = 91.3 ± 19.8%, $p_{Fmr1KO5} < 0.0001$, ci = [51.1-131.4], tstat: 4.62, df: 4, SD: 116.9; unpaired *t* test). Together, we found that, when inhibition is blocked, a larger magnitude LTD predominates in *Fmr1*KO PNs compared with WT mice (Fig. 5*C*). Importantly, we found a strong LTP response in *Fmr1*KO PNs when inhibition remains intact (Fig. 5*D*). Thus, significant bidirectional plasticity exists in the *Fmr1*KO mouse during a sensitive period in amygdala development, and *Fmr1*KO PNs undergo strong LTP in the presence of inhibition.

*Fmr1*KO mice exhibit emergence of fear conditioning before the known sensitive period

Given our observations of synaptic and microcircuit alterations during the BLA-sensitive period, we sought to examine the emergence of fear learning in the *Fmr1*KO mouse during the sensitive period (P10-P14 in mice). Since normal auditory processing in mouse pups emerges around the second postnatal week of life (Turner et al., 2005), it is not possible to use traditional auditory fear conditioning in P10 animals, and it is technically challenging to do this in P14 pups owing to their inability to navigate the foot shock grid and the potential for delivery of full-body shocks. However, early olfactory learning is necessary for the survival of infant rodents (Singh and Tobach, 1975) and developmental paradigms using olfactory CS-US learning are robust and well characterized in young animals (Perry et al., 2017). Therefore, we used a developmentally appropriate odor-shock fear conditioning paradigm to assay fear-learning across early postnatal development in *Fmr1*KO and WT mice. In this paradigm, mouse pups receive 8 pairings of exposure to a neutral odor (1% isoamyl acetate, CS) paired with a mild, 0.5 mA electric shock (US) delivered through an electrode placed on the tail. As a control, pups received either the presentation of the CS only or an unpaired presentation of CS and US. To assess fear conditioning, mouse pups were tested 24 h later for time spent in the two arms of a Y-maze (containing CS odor or socially familiar bed shavings) (Y-maze alteration test, Fig. 6*A*).

At P21, WT pups subjected to paired CS-US conditioning demonstrated a significant CS-aversion (Fig. 6*B*; Kruskal–Wallis ANOVA $F_{(2,51)} = 16.23$, $p = 0.0003$, MWU for *post hoc* analysis, α_{FDR} = 0.0286, $p_{WTpaired\_odor} < 0.0001$, zval: −3.20, rank-sum: 236.5, $p_{WTpaired\_unpaired}$ p =0.0014, zval: 3.20, rank-sum: 429.5, $p_{WTunpaired\_odor}$= 0.391, zval: −0.858, rank-sum: 308). Similarly, we observed significant differences between groups in P21 *Fmr1*KO pups (Fig. 6*B*; Kruskal–Wallis ANOVA $F_{(2,51)} = 23.75$, $p < 0.0001$, MWU for *post hoc* analysis, α_{FDR} = 0.0286, $p_{Fmr1KOpaired\_odor} < 0.0001$, zval: −4.26, rank-sum: 203.5, $p_{Fmr1KOpaired\_unpaired} < 0.0001$, zval: −4.07, rank-sum: 210.5, $p_{Fmr1KOunpaired\_odor}$= 0.619, zval: 0.497, rank-sum: 348). No differences in paired CS-US responses were observed between WT and *Fmr1*KO pups (Fig. 6*B*; MWU, α_{FDR} = 0.0250, $p = 0.672$, zval: 0.423, rank-sum: 346). At P14, we again observed significant differences between groups in P14 WT and *Fmr1*KO pups similar to P21 pups (Fig. 6*B*; WT P14, Kruskal–Wallis ANOVA $F_{(2,33)} = 8.48$, $p = 0.0144$, MWU for *post hoc* analysis, α_{FDR} = 0.0286, $p_{WTpaired\_odor}$= 0.0094, zval: −2.60, rank-sum: 106.5, $p_{WTpaired\_unpaired}$ = 0.0212, zval: −2.304, rank-sum: 110.5, $p_{WTunpaired\_odor}$= 0.8507, zval: 0.188, rank-sum: 153.5; *Fmr1*KO P14, Kruskal–Wallis ANOVA $F_{(2,33)} = 17.8$, $p = 0.0001$, MWU for *post hoc* analysis, α_{FDR} = 0.0286, $p_{Fmr1KOpaired\_odor} < 0.0001$, zval: −3.72, rank-sum: 87.0, $p_{Fmr1KOpaired\_unpaired}$ = 0.0022, zval: −3.06, rank-sum: 98.5, $p_{Fmr1KOunpaired\_odor}$= 0.1097, zval: 1.60, rank-sum: 174.5). Similarly, no differences in paired CS-US responses were observed between P14 WT and *Fmr1*KO pups (Fig. 6*B*; MWU, α_{FDR} = 0.0286, $p = 0.529$, zval: −0.630, rank-sum: 139).

In contrast, we found a striking difference in fear conditioning between *Fmr1*KO and WT mice at P10. In accordance with previous studies (Moriceau and Sullivan, 2005), P10 WT pups subjected to the paired CS-US condition demonstrated a paradoxical odor preference that was significantly different between groups (Fig. 6*B*; WT P10, Kruskal–Wallis ANOVA $F_{(2,33)} = 18.34$, $p = 0.0001$, MWU for *post hoc* analysis, α_{FDR} = 0.0357, $p_{WTpaired\_odor} < 0.0001$, zval: 3.89, rank-sum: 215, $p_{WTpaired\_unpaired} < 0.0001$, zval: 3.50, rank-sum: 209, $p_{WTunpaired\_odor}$= 0.9035, zval: 0.121, rank-sum: 152.5). However, *Fmr1*KO pups subjected to the paired CS-US condition instead demonstrated an odor-aversion (*Fmr1*KO P14, Kruskal–Wallis ANOVA $F_{(2,33)} = 16.21$, $p = 0.0003$, MWU for *post hoc* analysis, α_{FDR} = 0.0357, $p_{Fmr1KOpaired\_odor} < 0.0001$, zval: −3.54, rank-sum: 90, $p_{Fmr1KOpaired\_unpaired}$ = 0.0015, zval: −3.182, rank-sum: 96, $p_{Fmr1KOunpaired\_odor}$= 0.3389, zval: 0.956, rank-sum: 166). A significant difference between paired CS-US responses was observed between P10 WT and *Fmr1*KO pups (Fig. 5*B*; MWU, α_{FDR} = 0.0357, $p < 0.0001$, zval: −4.12, rank-sum: 80).

In light of our observation that fear-learning was broadly normal between P14-P16 WT and *Fmr1*KO mice, we asked whether fear-learning thresholds might be altered in the *Fmr1*KO mouse. Previous studies using odor-associated fear conditioning paradigms use ~8-12 CS-US pairings to induce strong odor-cued fear-learning (Valley et al., 2009). To examine threshold differences, we modified the above-described paradigm and reduced the CS-US presentations by half. Interestingly, a significant difference was observed between WT and *Fmr1*KO mice using four CS-US presentations. WT animals subjected to 4 CS + US presentations demonstrated a slight odor preference, and *Fmr1*KO

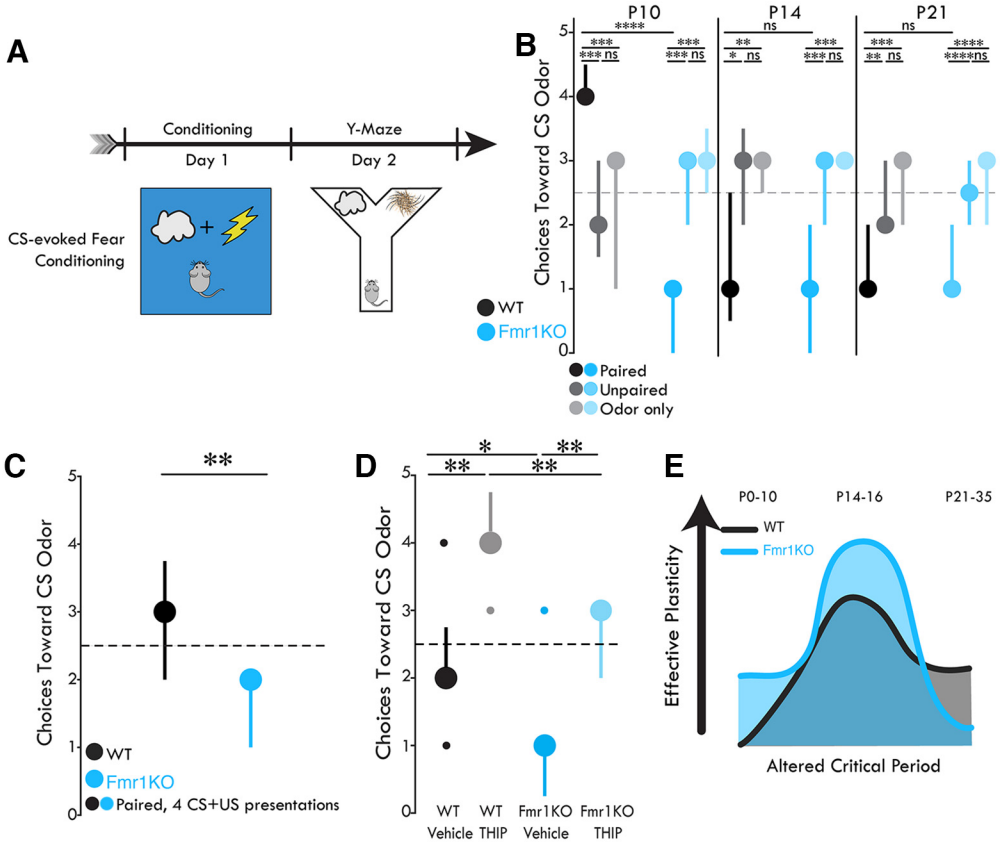

Figure 6. Precocious emergence of fear-learning in the Fmr1 KO mouse. ***A***, Experimental schematic. Complete statistical analyses are detailed in Results. ***B***, Fear-learning emerges before the P14-sensitive period in *Fmr1*KO mice (P10, P10 $n_{WT} = 12$ mice per condition, paired (P): 8 males, 4 females; unpaired (U): 7 males, 5 females; odor (0): 7 males, 5 females, 8 litters; $n_{Fmr1KO} =$ 12 mice per condition, P: 8 males, 4 females; U: 4 males, 8 females; 0: 6 males, 6 females, 9 litters; P14 $n_{WT} = 12$ mice per condition; P: 8 males, 4 females; U: 8 males, 4 females; 0: 9 males, 3 females, 8 litters; $n_{Fmr1KO} = 12$ mice per condition, P: 5 males, 7 females; U: 7 males, 5 females; 0: 10 males, 2 females, 8 litters; P21 $n_{WT} = 18$ mice per condition. P: 12 males, 6 females, U: 13 males 5 females; 0 only: 11 males 7 females, 12 litters; $n_{Fmr1KO} = 18$ mice per condition, P: 9 males, 9 females; U: 10 males, 8 females; 0: 12 males, 6 females, 12 litters). ***C***, Fear-learning thresholds are lower in P14 *Fmr1*KO mice (P14 $n_{WT} = 11$ mice, 6 males, 5 females, 3 litters, $n_{Fmr1KO} = 17$ mice, 10 males, 7 females, 3 litters). ***D***, THIP administration changes the valence of odor-cued fear-conditioning from odor aversion to odor preference in P14 WT and *Fmr1*KO mice (vehicle: P14 $n_{WT} = 7$ mice, 4 males 3 females, 3 litters, $n_{Fmr1KO} = 7$ mice, 5 males, 2 females, 3 litters; THIP: P14 $n_{WT} = 7$ mice, 5 males, 2 females, 3 litters, $n_{Fmr1KO} = 7$ mice, 4 males, 3 females, 3 litters). ***E***, Schematic concept-of-hypothesis of altered critical period plasticity in the FXS amygdala. Modified from Martin and Huntsman (2012). ***B***, ***C***, Summary statistics are median with IQR. $^*p < 0.05$. P10 = P8-P10; P14 = P14-P16. Complete statistical analyses are detailed in Results.

mouse pups continued to display a learned aversion (Fig. 6*C*; MWU, $p = 0.0042$, zval: 2.87, rank-sum: 218.5).

In order to evaluate the effect of enhancing tonic inhibition on odor-associated fear-conditioning, we administered systemic THIP or vehicle control (ddH_20) via intraperitoneal injection in P14 WT and *Fmr1*KO mice and examined fear-learning using the above-described paradigm. Surprisingly, we found that both WT and *Fmr1*KO THIP-treated animals demonstrated a valence switch in odor-learning wherein, in response to odor-cued fear-conditioning, WT and *Fmr1*KO animals demonstrated odor preferences instead of odor aversions (similar to animals at P10) compared with vehicle-treated controls. (Fig. 6*D*; Kruskal–Wallis ANOVA $F_{(3,24)} = 18{,}38$, $p = 0.0004$, MWU for *post hoc* analysis, $\alpha_{FDR} = 0.05$, $p_{WTcontrolVsWTthip} = 0.0064$, rank-sum: 31.5; $p_{WTthipVsFmr1KOthip} = 0.0029$, rank-sum: 75; $p_{Fmr1KOthipVsFmr1KOControl} = 0.0117$, rank-sum: 33; vehicle: P14 $n_{WT} = 7$ mice, 4 males, 3 females, 3 litters, $n_{Fmr1KO} = 7$ mice, 5 males, 2 females, 3; THIP: P14 $n_{WT} = 7$ mice, 5 males, 2 females, 3 litters, $n_{Fmr1KO} = 7$ mice, 4 males, 3 females, 3 litters). Significant differences were also observed between vehicle-treated WT and *Fmr1*KO pups demonstrating, as before, stronger aversion learning in *Fmr1*KO animals at P14 (Fig. 6*E*; MWU for *post hoc* analysis, $\alpha_{FDR} = 0.05$, $p_{WTcontrolVsFmr1KOcontrol} = 0.0181$, rank-sum: 35.5). Together, these data indicate that adult-like fear learning emerges precociously in the *Fmr1*KO mouse (Fig. 6*E*) and that fear-learning thresholds are altered in the P14-P16 *Fmr1*KO mouse. Further, systemic THIP treatment restores sensitive period odor-preferences in WT animals and ameliorates precocious fear-learning in *Fmr1*KO animals identifying a role for early life THIP intervention in FXS.

Discussion

A sensitive period is a transient window in the developing brain in NDDs wherein heightened plasticity exists outside of the normal CP of development (Martin and Huntsman, 2012; Meredith et al., 2012). Abnormal plasticity is a hallmark of NDDs, including FXS, but whether plasticity defects in the BLA are present at birth or emerge during development is unknown (Vislay et al., 2013). In the present study, we show that PNs within the BLA exhibit hyperexcitability during a sensitive period and that excitatory gain in fear-learning circuits is enhanced. This coincides with increases in inhibition which may represent an attempt to homeostatically balance changes in excitation in circuits

responsible for fear-learning. Further, increases in CP period plasticity are observed in the BLA. Behavioral correlation demonstrates that fear-learning emerges precociously in the *Fmr1*KO mouse. Indeed, an early life THIP intervention restores odor-cued preferences in WT animals and ameliorates fear-learning in *Fmr1*KO animals. These data suggest that the period of programmed synaptic and cellular changes required for normal circuit development and refinement in the FXS BLA occur earlier in development.

Hyperexcitable circuitry in the *Fmr1*KO BLA results from alterations in PN membrane intrinsic properties

Excitatory PNs in the BLA receive afferent input from the thalamus, lateral entorhinal cortex, and the cortical nucleus of the amygdala which drives plasticity in ensembles of excitatory PNs (Schoenbaum et al., 1999; Thompson et al., 2008; Nabavi et al., 2014; Barsy et al., 2020). This input encodes the emotional and motivational significance of the auditory or olfactory cues in associative learning (Grace and Rosenkranz, 2002). Importantly, hyperexcitable circuitry within the BLA has been postulated to underpin neuropsychiatric conditions in FXS and ASDs (Turk et al., 2005; Sharp, 2017). Here, we demonstrate P14 PNs in the *Fmr1*KO BLA exhibit increased FRs, a lower rheobase, and depolarized RMPs. This finding is in accordance with previous studies demonstrating hyperexcitability in cortical and hippocampal PNs (Goncalves et al., 2013; Y. Zhang et al., 2014; Routh et al., 2017; Z. Zhang et al., 2018). Interestingly, we also observed alterations in AP broadening. AP broadening is a major facilitator of frequency-dependent Ca^{2+} dynamics with implications for enhancements of LTP (Jackson et al., 1991). Within the BLA, Ca^{2+} activated K^+ (BK) channels have been shown to be primarily responsible for frequency-dependent spike broadening (Faber and Sah, 2003). Importantly, FMRP has a known role in translation-independent modulation of BK channels (Deng et al., 2013). Indeed, BK channel dysfunction has been shown in *Fmr1*KO hippocampal PNs to drive AP broadening, enhance presynaptic calcium influx and neurotransmitter release at the synapse (Deng and Klyachko, 2016). Thus, it stands to reason that BK channelopathies may be present in BLA PNs. Future studies will be needed to address which ion channels are affected in the *Fmr1*KO BLA in early development.

Functional inhibitory neurotransmission is enhanced in the context of increased excitatory gain in *Fmr1*KO BLA

In multiple brain regions, the biophysical properties of IPSCs follow a patterned developmental maturation in the first 3 weeks of life (Tia et al., 1996; Hollrigel and Soltesz, 1997; Dunning et al., 1999; Huntsman and Huguenard, 2000). Interestingly, our published work identified alterations in the developmental maturation of inhibitory neurotransmission in *Fmr1*KO mice (Vislay et al., 2013). Here, we extend these findings to include transient increases in tonic inhibition. Interestingly, these changes in inhibitory neurotransmission occur in the absence of changes in excitatory synaptic strength or kinetics. Tonic inhibition has been shown to be a potent modulator of excitability in somatostatin-expressing interneurons (Bryson et al., 2020). Our group has shown that FFI in the BLA is mediated by SST-expressing interneurons, particularly in circuits necessary for olfactory learning (Guthman et al., 2018, 2020). Thus, increases in tonic inhibition may function to enhance FFI in a homeostatic manner. Conversely, recent work has demonstrated that chronic stress and exogeneous corticosterone administration increases tonic inhibition in Thy1-expressing neurons in the LA (Pan et al., 2020). Importantly, Thy1-expressing neurons have been shown to mediate fear inhibition and extinction (Jasnow et al., 2013). Thus, increases in tonic inhibition in these cells could function to paradoxically enhance fear-learning. More rigorous investigations of tonic inhibition will be needed to determine whether changes in tonic inhibition affect E/I balance in a cell type-specific manner or apply more broadly.

Previous studies of neocortical E/I balance in early development have found a preferential reduction in feedback inhibition. Interestingly, feedforward inhibition is unaffected. Accordingly, in our study, FFI onto BLA PNs in the *Fmr1*KO mouse is broadly normal at P14. However, we observe an increase in excitatory gain in the context of intact FFI. In V1, large voltage-gated conductances have been shown to increase membrane resistance with depolarization and that this affects the input–output relationship such that gain and subthreshold selectivity is enhanced (B. Li et al., 2020). We postulate that a similar phenomenon may exist in the BLA. In particular, we find that PNs in the BLA exhibit increased membrane resistance as well as a more depolarized RMP. Thus, the overall net effect of altered intrinsic properties may be to alter the input–output function in the *Fmr1*KO BLA such that significant increases in excitatory gain are present in circuits necessary for fear-learning. We propose that increases seen in phasic and tonic inhibitory neurotransmission at P14-P16 are likely a homeostatic response to restore E/I balance. However, this homeostatic correction may not be completely effective. Together, this may result in lower thresholds for fear-learning such that lesser stimuli result in robust fear-learning in patients with FXS and ASDs. However, we cannot rule out long-range connectivity changes, especially under subthreshold threat response conditioning (Kirry et al., 2020).

Hyperexcitable circuitry contributes to pathologic plasticity in circuits important for fear-learning

Previous studies of amygdala function in mouse models of FXS and human patients with FXS have demonstrated inconsistent results (Garrett et al., 2004; Watson et al., 2008; Kim et al., 2014). One possible explanation for this is that these studies necessarily focused on older children, adolescents, or adults. Similarly, in mouse models of FXS, plasticity studies have routinely been performed in aged mice with reductions in both long- and short-term synaptic plasticity observed in the BLA (Zhao et al., 2005; Suvrathan et al., 2010). However, other studies have demonstrated enhancement of early life LTP in the hippocampus in *Fmr1*KO mice (Pilpel et al., 2009). To our knowledge, similar early developmental plasticity studies have not been conducted in the *Fmr1*KO BLA. Importantly, changes in plasticity have been shown to underpin the developmental emergence of mature adult-like amygdala function (Thompson et al., 2008). Interestingly, under conditions of GABA receptor blockade, LTD predominates, demonstrating that immature GABA exhibits a strong influence on synaptic plasticity in the neonatal amygdala. In accordance with this study, we observed an enhancement of synaptic plasticity that is dependent on the state of inhibition. With inhibitory blockade, we observed LTD in *Fmr1*KO PNs in the BLA. Conversely, under conditions of intact inhibition, we observe robust and sustained LTP in *Fmr1*KO PNs in the BLA compared with WT animals. LTP within in the BLA was been shown to be mediated by numerous mechanisms, including dendritic R-voltage-dependent calcium channel Ca^{2+} spikes (Humeau and Luthi, 2007), Group 1 mGluR-mediated enhancement of R-voltage-dependent calcium channels (Gray et al., 2019), AMPAR subunit GluA2, and altered NMDAR/AMPA ratios

(Banke and Barria, 2020). Future studies will be needed to dissect the mechanistic basis by which plasticity is enhanced to identify therapeutic targets.

Precocious emergence of adult-like functioning of the amygdala

Previous studies examining fear-learning in adult *Fmr1*KO mice have demonstrated reductions in responses during contextual and cued fear-learning (Paradee et al., 1999). While the development of fear-learning in rodent models is well characterized, few studies have addressed fear-learning in early development in mouse models of FXS or ASDs. Young altricial infants (~P10), defenseless and confined to the nest, rely on the parental protection with an age-specific approach to the parent as a typical response to threat coupled with suppression of fear learning (Bowlby, 1982). Thus, at P10, the olfactory fear conditioning paradigm induces a preference for the odor cue in WT pups (Sullivan et al., 2000; Opendak et al., 2019), which we replicate here. Our *Fmr1*KO results show that this early sensitive period is precociously terminated likely because of altered E/I balance and enhancements in BLA LTP. Typically, this developmental transition occurs as pups develop gross motor skills to make brief excursions out of the nest. Since *Fmr1*KO mice do not show accelerated motor development, this precocious fear learning may be one of the first signs of a disruption in the delicate balance of coordinated neurobehavioral development.

With maturation and preparation for independence (~P14), a system of amygdala-dependent fear-learning and self-defense emerges. At this time, infant and adult-like systems coexist, with parental presence engaging the infant system and parental absence engaging the amygdala-dependent fear-learning (Moriceau and Sullivan, 2006; Moriceau et al., 2006; Tottenham et al., 2019). This neurobehavioral fear transition has been documented across species (Ganella and Kim, 2014; Gunnar et al., 2015; Hartley and Lee, 2015; Pattwell and Bath, 2017; Callaghan et al., 2019; McLaughlin et al., 2019; Tottenham et al., 2019; Sullivan and Opendak, 2021). Careful assessment demonstrates that fear-learning thresholds are altered in the *Fmr1*KO animal at this time point. Interestingly, administration of THIP restored a preference for the odor cue in WT animals and ameliorated fear-learning in *Fmr1*KO mice. This identifies a novel role for tonic inhibition mediated by $GABA_A$ receptor subunits (e.g., δ and $\alpha 3$ subunits) in CP plasticity. Indeed, tonic inhibition robustly induces CP plasticity in visual cortex (Iwai et al., 2003). Of note, because THIP was systemically administered, it is not possible to conclude that THIP modulates suppression of fear-learning through a unique effect in the BLA. Thus, future studies using focal manipulations in the BLA are warranted. It should also be noted that male and female animals are not equally represented in our dataset. Thus, this precludes a rigorous sex difference analysis. However, previous studies of hemizygous male and homozygous female mice (as used in this study) demonstrated no differences across a range of behavioral paradigms (Baker et al., 2010; Ding et al., 2014). Further, our own studies demonstrated no differences in plasticity (Svalina et al., 2021). This evidence suggests that sex differences may not be the primary driver of the pathology seen in *Fmr1*KO mice. However, given the sex bias found in NDDs, future studies rigorously assessing sex differences are warranted.

References

Baker KB, Wray SP, Ritter R, Mason S, Lanthorn TH, Savelieva KV (2010) Male and female Fmr1 knockout mice on C57 albino background exhibit spatial learning and memory impairments. Genes Brain Behav 9:562–574.

Banke TG, Barria A (2020) Transient enhanced GluA2 expression in young hippocampal neurons of a Fragile X mouse model. Front Synaptic Neurosci 12:588295.

Barsy B, Kocsis K, Magyar A, Babiczky A, Szabo M, Veres JM, Hillier D, Ulbert I, Yizhar O, Matyas F (2020) Associative and plastic thalamic signaling to the lateral amygdala controls fear behavior. Nat Neurosci 23:625–637.

Bonaccorso CM, Spatuzza M, Di Marco B, Gloria A, Barrancotto G, Cupo A, Musumeci SA, D'Antoni S, Bardoni B, Catania MV (2015) Fragile X mental retardation protein (FMRP) interacting proteins exhibit different expression patterns during development. Int J Dev Neurosci 42:15–23.

Borsini F, Evangelista S, Meli A (1986) Effect of GABAergic drugs in the behavioral 'despair' test in rats. Eur J Pharmacol 121:265–268.

Bowlby J (1982) Attachment and loss: retrospect and prospect. Am J Orthopsychiatry 52:664–678.

Bryson A, Hatch RJ, Zandt BJ, Rossert C, Berkovic SF, Reid CA, Grayden DB, Hill SL, Petrou S (2020) GABA-mediated tonic inhibition differentially modulates gain in functional subtypes of cortical interneurons. Proc Natl Acad Sci USA 117:3192–3202.

Bureau I, Shepherd GM, Svoboda K (2008) Circuit and plasticity defects in the developing somatosensory cortex of FMR1 knock-out mice. J Neurosci 28:5178–5188.

Callaghan B, Meyer H, Opendak M, Van Tieghem M, Harmon C, Li A, Lee FS, Sullivan RM, Tottenham N (2019) Using a developmental ecology framework to align fear neurobiology across species. Annu Rev Clin Psychol 15:345–369.

Cea-Del Rio CA, Huntsman MM (2014) The contribution of inhibitory interneurons to circuit dysfunction in Fragile X syndrome. Front Cell Neurosci 8:245.

Chaudhury S, Sharma V, Kumar V, Nag TC, Wadhwa S (2016) Activity-dependent synaptic plasticity modulates the critical phase of brain development. Brain Dev 38:355–363.

Chen L, Yun SW, Seto J, Liu W, Toth M (2003) The fragile X mental retardation protein binds and regulates a novel class of mRNAs containing U rich target sequences. Neuroscience 120:1005–1017.

Contractor A, Klyachko VA, Portera-Cailliau C (2015) Altered neuronal and circuit excitability in Fragile X syndrome. Neuron 87:699–715.

Cordeiro L, Ballinger E, Hagerman R, Hessl D (2011) Clinical assessment of DSM-IV anxiety disorders in fragile X syndrome: prevalence and characterization. J Neurodev Disord 3:57–67.

Curran-Everett D (2000) Multiple comparisons: philosophies and illustrations. Am J Physiol Regul Integr Comp Physiol 279:R1–8.

Darnell JC, Klann E (2013) The translation of translational control by FMRP: therapeutic targets for FXS. Nat Neurosci 16:1530–1536.

Darnell JC, Van Driesche SJ, Zhang C, Hung KY, Mele A, Fraser CE, Stone EF, Chen C, Fak JJ, Chi SW, Licatalosi DD, Richter JD, Darnell RB (2011) FMRP stalls ribosomal translocation on mRNAs linked to synaptic function and autism. Cell 146:247–261.

Deng PY, Rotman Z, Blundon JA, Cho Y, Cui J, Cavalli V, Zakharenko SS, Klyachko VA (2013) FMRP regulates neurotransmitter release and synaptic information transmission by modulating action potential duration via BK channels. Neuron 77:696–711.

Deng PY, Klyachko VA (2016) Genetic upregulation of BK channel activity normalizes multiple synaptic and circuit defects in a mouse model of fragile X syndrome. J Physiol 594:83–97.

Ding Q, Sethna F, Wang H (2014) Behavioral analysis of male and female Fmr1 knockout mice on C57BL/6 background. Behav Brain Res 271:72–78.

Doll CA, Broadie K (2015) Activity-dependent FMRP requirements in development of the neural circuitry of learning and memory. Development 142:1346–1356.

Dunning DD, Hoover CL, Soltesz I, Smith MA, O'Dowd DK (1999) GABA (A) receptor-mediated miniature postsynaptic currents and alpha-subunit expression in developing cortical neurons. J Neurophysiol 82:3286–3297.

Faber ES, Sah P (2003) Ca^{2+}-activated K^+ (BK) channel inactivation contributes to spike broadening during repetitive firing in the rat lateral amygdala. J Physiol 552:483–497.

Fu YH, Kuhl DP, Pizzuti A, Pieretti M, Sutcliffe JS, Richards S, Verkerk AJ, Holden JJ, Fenwick RG Jr, Warren ST (1991) Variation of the CGG repeat at the fragile X site results in genetic instability: resolution of the Sherman paradox. Cell 67:1047–1058.

Ganella DE, Kim JH (2014) Developmental rodent models of fear and anxiety: from neurobiology to pharmacology. Br J Pharmacol 171:4556–4574.

Garrett AS, Menon V, MacKenzie K, Reiss AL (2004) Here's looking at you, kid: neural systems underlying face and gaze processing in fragile X syndrome. Arch Gen Psychiatry 61:281–288.

Goncalves JT, Anstey JE, Golshani P, Portera-Cailliau C (2013) Circuit level defects in the developing neocortex of Fragile X mice. Nat Neurosci 16:903–909.

Grace AA, Rosenkranz JA (2002) Regulation of conditioned responses of basolateral amygdala neurons. Physiol Behav 77:489–493.

Gray EE, Murphy JG, Liu Y, Trang I, Tabor GT, Lin L, Hoffman DA (2019) Disruption of GpI mGluR-dependent Cav2.3 translation in a mouse model of Fragile X syndrome. J Neurosci 39:7453–7464.

Gunnar MR, Hostinar CE, Sanchez MM, Tottenham N, Sullivan RM (2015) Parental buffering of fear and stress neurobiology: reviewing parallels across rodent, monkey, and human models. Soc Neurosci 10:474–478.

Guthman EM, Ma M, Chu P, Baca SM, Restrepo D, Huntsman MM (2018) Cell type specific control of basolateral amygdala plasticity via entorhinal cortex-driven feedforward inhibition. Available at https://ssrn.com/abstract=3272233.

Guthman EM, Garcia JD, Ma M, Chu P, Baca SM, Smith KR, Restrepo D, Huntsman MM (2020) Cell-type-specific control of basolateral amygdala neuronal circuits via entorhinal cortex-driven feedforward inhibition. Elife 9:e50601.

Hagerman RJ, Berry-Kravis E, Kaufmann WE, Ono MY, Tartaglia N, Lachiewicz A, Kronk R, Delahunty C, Hessl D, Visootsak J, Picker J, Gane L, Tranfaglia M (2009) Advances in the treatment of fragile X syndrome. Pediatrics 123:378–390.

Harlow EG, Till SM, Russell TA, Wijetunge LS, Kind P, Contractor A (2010) Critical period plasticity is disrupted in the barrel cortex of Fmr1 knockout mice. Neuron 65:385–398.

Hartley CA, Lee FS (2015) Sensitive periods in affective development: nonlinear maturation of fear learning. Neuropsychopharmacology 40:50–60.

He Q, Nomura T, Xu J, Contractor A (2014) The developmental switch in GABA polarity is delayed in fragile X mice. J Neurosci 34:446–450.

Hollrigel GS, Soltesz I (1997) Slow kinetics of miniature IPSCs during early postnatal development in granule cells of the dentate gyrus. J Neurosci 17:5119–5128.

Huber KM, Gallagher SM, Warren ST, Bear MF (2002) Altered synaptic plasticity in a mouse model of fragile X mental retardation. Proc Natl Acad Sci USA 99:7746–7750.

Humeau Y, Luthi A (2007) Dendritic calcium spikes induce bi-directional synaptic plasticity in the lateral amygdala. Neuropharmacology 52:234–243.

Huntsman MM, Huguenard JR (2000) Nucleus-specific differences in GABA (A)-receptor-mediated inhibition are enhanced during thalamic development. J Neurophysiol 83:350–358.

Iwai Y, Fagiolini M, Obata K, Hensch TK (2003) Rapid critical period induction by tonic inhibition in visual cortex. J Neurosci 23:6695–6702.

Jackson MB, Konnerth A, Augustine GJ (1991) Action potential broadening and frequency-dependent facilitation of calcium signals in pituitary nerve terminals. Proc Natl Acad Sci USA 88:380–384.

Jasnow AM, Ehrlich DE, Choi DC, Dabrowska J, Bowers ME, McCullough KM, Rainnie DG, Ressler KJ (2013) Thy1-expressing neurons in the basolateral amygdala may mediate fear inhibition. J Neurosci 33:10396–10404.

Kim SY, Burris J, Bassal F, Koldewyn K, Chattarji S, Tassone F, Hessl D, Rivera SM (2014) Fear-specific amygdala function in children and adolescents on the fragile x spectrum: a dosage response of the FMR1 gene. Cereb Cortex 24:600–613.

Kirry AJ, Twining RC, Gilmartin MR (2020) Prelimbic input to basolateral amygdala facilitates the acquisition of trace cued fear memory under weak training conditions. Neurobiol Learn Mem 172:107249.

Li A, Gire DH, Restrepo D (2015) Upsilon spike-field coherence in a population of olfactory bulb neurons differentiates between odors irrespective of associated outcome. J Neurosci 35:5808–5822.

Li B, Routh BN, Johnston D, Seidemann E, Priebe NJ (2020) Voltage-gated intrinsic conductances shape the input–output relationship of cortical neurons in behaving primate V1. Neuron 107:185–196.e4.

Liu XS, Wu H, Krzisch M, Wu X, Graef J, Muffat J, Hnisz D, Li CH, Yuan B, Xu C, Li Y, Vershkov D, Cacace A, Young RA, Jaenisch R (2018) Rescue of Fragile X syndrome neurons by DNA methylation editing of the FMR1 gene. Cell 172:979–992.e976.

Martin BS, Huntsman MM (2012) Pathological plasticity in fragile X syndrome. Neural Plast 2012:275630.

Martin BS, Corbin JG, Huntsman MM (2014) Deficient tonic GABAergic conductance and synaptic balance in the fragile X syndrome amygdala. J Neurophysiol 112:890–902.

McKernan MG, Shinnick-Gallagher P (1997) Fear conditioning induces a lasting potentiation of synaptic currents in vitro. Nature 390:607–611.

McLaughlin KA, DeCross SN, Jovanovic T, Tottenham N (2019) Mechanisms linking childhood adversity with psychopathology: learning as an intervention target. Behav Res Ther 118:101–109.

Meredith RM (2015) Sensitive and critical periods during neurotypical and aberrant neurodevelopment: a framework for neurodevelopmental disorders. Neurosci Biobehav Rev 50:180–188.

Meredith RM, Holmgren CD, Weidum M, Burnashev N, Mansvelder HD (2007) Increased threshold for spike-timing-dependent plasticity is caused by unreliable calcium signaling in mice lacking fragile X gene FMR1. Neuron 54:627–638.

Meredith RM, Dawitz J, Kramvis I (2012) Sensitive time-windows for susceptibility in neurodevelopmental disorders. Trends Neurosci 35:335–344.

Moriceau S, Sullivan RM (2005) Neurobiology of infant attachment. Dev Psychobiol 47:230–242.

Moriceau S, Sullivan RM (2006) Maternal presence serves as a switch between learning fear and attraction in infancy. Nat Neurosci 9:1004–1006.

Moriceau S, Wilson DA, Levine S, Sullivan RM (2006) Dual circuitry for odor-shock conditioning during infancy: corticosterone switches between fear and attraction via amygdala. J Neurosci 26:6737–6748.

Murthy S, Gould E (2018) Early life stress in rodents: animal models of illness or resilience? Front Behav Neurosci 12:157.

Nabavi S, Fox R, Proulx CD, Lin JY, Tsien RY, Malinow R (2014) Engineering a memory with LTD and LTP. Nature 511:348–352.

Nelson SB, Valakh V (2015) Excitatory/inhibitory balance and circuit homeostasis in autism spectrum disorders. Neuron 87:684–698.

Olmos-Serrano JL, Paluszkiewicz SM, Martin BS, Kaufmann WE, Corbin JG, Huntsman MM (2010) Defective GABAergic neurotransmission and pharmacological rescue of neuronal hyperexcitability in the amygdala in a mouse model of fragile X syndrome. J Neurosci 30:9929–9938.

Olmos-Serrano JL, Corbin JG, Burns MP (2011) The GABA (A) receptor agonist THIP ameliorates specific behavioral deficits in the mouse model of fragile X syndrome. Dev Neurosci 33:395–403.

Opendak M, Robinson-Drummer P, Blomkvist A, Zanca RM, Wood K, Jacobs L, Chan S, Tan S, Woo J, Venkataraman G, Kirschner E, Lundstrom JN, Wilson DA, Serrano PA, Sullivan RM (2019) Neurobiology of maternal regulation of infant fear: the role of mesolimbic dopamine and its disruption by maltreatment. Neuropsychopharmacology 44:1247–1257.

Paluszkiewicz SM, Martin BS, Huntsman MM (2011) Fragile X syndrome: the GABAergic system and circuit dysfunction. Dev Neurosci 33:349–364.

Pan HQ, Zhang WH, Liao CZ, He Y, Xiao ZM, Qin X, Liu WZ, Wang N, Zou JX, Liu XX, Pan BX (2020) Chronic stress oppositely regulates tonic inhibition in Thy1-expressing and non-expressing neurons in amygdala. Front Neurosci 14:299.

Paradee W, Melikian HE, Rasmussen DL, Kenneson A, Conn PJ, Warren ST (1999) Fragile X mouse: strain effects of knockout phenotype and evidence suggesting deficient amygdala function. Neuroscience 94:185–192.

Pattwell SS, Bath KG (2017) Emotional learning, stress, and development: an ever-changing landscape shaped by early-life experience. Neurobiol Learn Mem 143:36–48.

Perry RE, Blair C, Sullivan RM (2017) Neurobiology of infant attachment: attachment despite adversity and parental programming of emotionality. Curr Opin Psychol 17:1–6.

Pilpel Y, Kolleker A, Berberich S, Ginger M, Frick A, Mientjes E, Oostra BA, Seeburg PH (2009) Synaptic ionotropic glutamate receptors and plasticity are developmentally altered in the CA1 field of Fmr1 knockout mice. J Physiol 587:787–804.

Routh BN, Rathour RK, Baumgardner ME, Kalmbach BE, Johnston D, Brager DH (2017) Increased transient Na (+) conductance and action potential output in layer 2/3 prefrontal cortex neurons of the fmr1 (-/y) mouse. J Physiol 595:4431–4448.

Rubenstein JL, Merzenich MM (2003) Model of autism: increased ratio of excitation/inhibition in key neural systems. Genes Brain Behav 2:255–267.

Sah P, Faber ES, Lopez De Armentia M, Power J (2003) The amygdaloid complex: anatomy and physiology. Physiol Rev 83:803–834.

Schoenbaum G, Chiba AA, Gallagher M (1999) Neural encoding in orbitofrontal cortex and basolateral amygdala during olfactory discrimination learning. J Neurosci 19:1876–1884.

Semyanov A, Walker MC, Kullmann DM, Silver RA (2004) Tonically active GABA A receptors: modulating gain and maintaining the tone. Trends Neurosci 27:262–269.

Sharp BM (2017) Basolateral amygdala and stress-induced hyperexcitability affect motivated behaviors and addiction. Transl Psychiatry 7:e1194.

Singh PJ, Tobach E (1975) Olfactory bulbectomy and nursing behavior in rat pups (Wistar DAB). Dev Psychobiol 8:151–164.

Sullivan RM, Opendak M (2021) Neurobiology of infant fear and anxiety: impacts of delayed amygdala development and attachment figure quality. Biol Psychiatry 89:641–650.

Sullivan RM, Landers M, Yeaman B, Wilson DA (2000) Good memories of bad events in infancy. Nature 407:38–39.

Suvrathan A, Hoeffer CA, Wong H, Klann E, Chattarji S (2010) Characterization and reversal of synaptic defects in the amygdala in a mouse model of fragile X syndrome. Proc Natl Acad Sci USA 107:11591–11596.

Svalina MN, Guthman EM, Cea-Del Rio CA, Kushner JK, Baca SM, Restrepo D, Huntsman MM (2021) Hyperexcitability and loss of feedforward inhibition contribute to aberrant plasticity in the Fmr1KO amygdala. eNeuro 8:ENEURO.0113-21.2021.

Tessier CR, Broadie K (2008) *Drosophila* fragile X mental retardation protein developmentally regulates activity-dependent axon pruning. Development 135:1547–1557.

Thompson JV, Sullivan RM, Wilson DA (2008) Developmental emergence of fear learning corresponds with changes in amygdala synaptic plasticity. Brain Res 1200:58–65.

Tia S, Wang JF, Kotchabhakdi N, Vicini S (1996) Developmental changes of inhibitory synaptic currents in cerebellar granule neurons: role of GABA (A) receptor alpha 6 subunit. J Neurosci 16:3630–3640.

Till SM (2010) The developmental roles of FMRP. Biochem Soc Trans 38:507–510.

Todrank J, Heth G, Restrepo D (2011) Effects of in utero odorant exposure on neuroanatomical development of the olfactory bulb and odour preferences. Proc Biol Sci 278:1949–1955.

Tottenham N, Shapiro M, Flannery J, Caldera C, Sullivan RM (2019) Parental presence switches avoidance to attraction learning in children. Nat Hum Behav 3:1070–1077.

Tsiouris JA, Brown WT (2004) Neuropsychiatric symptoms of fragile X syndrome: pathophysiology and pharmacotherapy. CNS Drugs 18:687–703.

Turk J, Robbins I, Woodhead M (2005) Post-traumatic stress disorder in young people with intellectual disability. J Intellect Disabil Res 49:872–875.

Turner JG, Parrish JL, Hughes LF, Toth LA, Caspary DM (2005) Hearing in laboratory animals: strain differences and nonauditory effects of noise. Comp Med 55:12–23.

Valley MT, Mullen TR, Schultz LC, Sagdullaev BT, Firestein S (2009) Ablation of mouse adult neurogenesis alters olfactory bulb structure and olfactory fear conditioning. Front Neurosci 3:51.

Verkerk AJ, Pieretti M, Sutcliffe JS, Fu YH, Kuhl DP, Pizzuti A, Reiner O, Richards S, Victoria MF, Zhang FP (1991) Identification of a gene (FMR-1) containing a CGG repeat coincident with a breakpoint cluster region exhibiting length variation in fragile X syndrome. Cell 65:905–914.

Vislay RL, Martin BS, Olmos-Serrano JL, Kratovac S, Nelson DL, Corbin JG, Huntsman MM (2013) Homeostatic responses fail to correct defective amygdala inhibitory circuit maturation in fragile X syndrome. J Neurosci 33:7548–7558.

Watson C, Hoeft F, Garrett AS, Hall SS, Reiss AL (2008) Aberrant brain activation during gaze processing in boys with fragile X syndrome. Arch Gen Psychiatry 65:1315–1323.

Zha XM (2013) Acid-sensing ion channels: trafficking and synaptic function. Mol Brain 6:1.

Zhang Y, Bonnan A, Bony G, Ferezou I, Pietropaolo S, Ginger M, Sans N, Rossier J, Oostra B, LeMasson G, Frick A (2014) Dendritic channelopathies contribute to neocortical and sensory hyperexcitability in Fmr1 (-/y) mice. Nat Neurosci 17:1701–1709.

Zhang Z, Marro SG, Zhang Y, Arendt KL, Patzke C, Zhou B, Fair T, Yang N, Sudhof TC, Wernig M, Chen L (2018) The fragile X mutation impairs homeostatic plasticity in human neurons by blocking synaptic retinoic acid signaling. Sci Transl Med 10:eaar4388.

Zhao MG, Toyoda H, Ko SW, Ding HK, Wu LJ, Zhuo M (2005) Deficits in trace fear memory and long-term potentiation in a mouse model for fragile X syndrome. J Neurosci 25:7385–7392.